J Adv Ceram

Research Article

A high-entropy rare-earth phosphate and its principle single component $REPO_4$ for environmental barrier coatings

Bishnu Pada Majee[1,2], Keith Bryce[2], Liping Huang[1,✉], Jie Lian[1,2,✉]

Cite this article: Majee B, Bryce K, Huang L, et al. *J Adv Ceram* 2025, **14**(3): 9221041. https://doi.org/10.26599/JAC.2025.9221041

ABSTRACT: Xenotime rare-earth (RE) phosphates are emerging as promising materials for environmental barrier coatings (EBCs) for SiC-based ceramic–matrix composites (CMCs) because of their close coefficients of thermal expansion (CTEs) and resistance to calcium–magnesium–alumina-silicate (CMAS) corrosion. In this work, high-entropy (HE) $(Sc_{0.2}Lu_{0.2}Yb_{0.2}Er_{0.2}Y_{0.2})PO_4$ and five single-component $REPO_4$ (RE = Sc, Lu, Yb, Er, and Y) compounds were synthesized, and their stability, thermal properties, and CMAS corrosion resistance were investigated. The CTE values of four $REPO_4$ compounds (RE = Lu, Yb, Er, and Y; ~(5.6–6)×10^{-6} °C^{-1}) are close to those of SiC–CMC ((4.5–5.5)×10^{-6} °C^{-1}), whereas $ScPO_4$ (6.98×10^{-6} °C^{-1}) and HE $(5RE_{0.2})PO_4$ (6.39×10^{-6} °C^{-1}) have slightly higher values in the temperature range of 200–1300 °C. HE phosphate has the lowest thermal conductivity due to its size and mass disorder. Systematic CMAS corrosion tests at 1300 °C for 5, 45, and 96 h revealed that all RE phosphates formed a continuous and dense reaction layer predominantly composed of $Ca_8MgRE(PO_4)_7$, effectively impeding CMAS penetration. Additionally, $REPO_4$ with smaller RE^{3-} cations displays a slower reaction rate and reduced corrosion kinetics, as evidenced by the smaller thickness of the reaction layer. A larger negative difference in the optical basicity (OB) value between $REPO_4$ and CMAS signifies greater corrosion resistance. A mechanistic understanding of CMAS corrosion and elucidation of the effects of critical parameters such as the ionic mass and ionic radius of RE elements on their thermal properties and CMAS corrosion kinetics are useful for the development of novel xenotime-type phosphates as EBCs for SiC–CMCs.

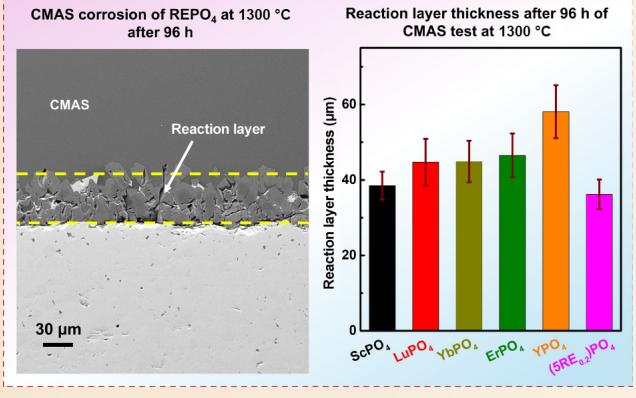

KEYWORDS: environmental barrier coatings (EBCs); rare-earth (RE) phosphate; coefficients of thermal expansion (CTEs); thermal conductivity; calcium–magnesium–alumina–silicate (CMAS) corrosion

1 Introduction

The desire to increase engine operational temperatures to increase fuel efficiency, performance, and durability is the forthcoming trajectory in the evolution of gas turbine engines [1,2]. The operating temperature of a gas turbine engine can be increased by replacing nickel-based superalloys with SiC-based ceramic matrix composites (CMCs) [3,4]. Compared with conventional Ni-base superalloys, SiC–CMCs have outstanding properties, such as low density, increased oxidation resistance, outstanding mechanical properties, and high melting points [4–6]. CMCs are currently being used in the hot section of gas turbine engines that can operate at relatively high temperatures, surpassing the melting point of superalloys (T > 1350 °C). However, under a combustion environment at high temperatures, SiC–CMC can be oxidized, resulting in the formation of a thermally grown SiO_2 layer [7], which interacts with water vapor under high-velocity gas steam conditions to form $Si(OH)_4$ gas according to Reaction (1), leading to recession and reducing the lifespan of SiC–CMCs.

$$SiO_2(s) + 2H_2O(g) \rightarrow Si(OH)_4(g) \quad (1)$$

During takeoff and landing of an aircraft, siliceous oxides such as volcano ash, sand, and dust enter the engine to form molten calcium–magnesium–alumina-silicate (CMAS) when the temperature exceeds 1200 °C [8] and interact with SiC–CMCs [9]. This interaction between molten CMAS and SiC–CMCs at high temperatures and in an oxidative environment results in the recession of SiC–CMC components in the long-term process [10]. Hence, to protect SiC–CMC from water vapor and CMAS corrosion, environmental barrier coatings (EBCs) have been proposed to improve the high-temperature tolerance and extend

[1] Department of Materials Science and Engineering, Rensselaer Polytechnic Institute, NY 12180, USA. [2] Department of Mechanical, Aerospace and Nuclear Engineering, Rensselaer Polytechnic Institute, NY 12180, USA.

✉ Corresponding authors. E-mail: L. Huang, huangl5@rpi.edu; J. Lian, lianj@rpi.edu

Received: November 13, 2024; Revised: January 7, 2025; Accepted: January 23, 2025

the service life of SiC–CMCs. The current generation EBCs are rare earth (RE) silicate materials with excellently matched coefficients of thermal expansion (CTEs) with SiC–CMCs and low thermal conductivities [11–14]. Studies have been conducted on CMAS corrosion of RE silicates [15,16] to understand the effect of the REE radius on CMAS corrosion [12,17–19]. For example, Tian *et al.* [20] investigated the effect of the ionic radius of REEs on mono-silicate, RE_2SiO_5–CMAS interactions at 1300 °C for 50 h and reported that an oxyapatite crystalline phase formed at the interface of CMAS and RE_2SiO_5 (RE = Tm, Yb, Lu, Tb, Dy, and Ho) and that the thickness of the reaction layer decreased with decreasing ionic radius of the REEs. However, their stability under CMAS and water vapor corrosion is not optimal at high temperatures because of the volatility of Si in rare earth silicates ($RE_2Si_2O_7$/RE_2SiO_5).

To overcome these challenges, single- and multicomponent monazite/xenotime-type rare earth phosphates ($REPO_4$) were recently proposed as advanced EBCs, and their thermal properties and CMAS corrosion resistance were investigated [21–24]. In particular, xenotime RE phosphates have been reported to have CTEs closely matched with SiC–CMCs, high-temperature stability, and good CMAS corrosion resistance [22,23]. For example, Wang *et al.* [21] synthesized three different monazite phosphates, $LnPO_4$ (Ln = Nd, Sm, and Gd), via a chemical route and studied CMAS corrosion at 1250 °C. Their results revealed that, among the three phosphates, $GdPO_4$ exhibited the best CMAS resistance because of the smaller ionic size of Gd^{3+}. However, most studies on xenotime $REPO_4$ have focused primarily on the corrosion behavior of $LuPO_4$, $YbPO_4$, and multicomponent phosphates, with a limited understanding of the corrosion mechanisms across different RE elements at 1300 °C [22,23,25,26].

In this work, a novel high-entropy (HE) $(5RE_{0.2})PO_4$ rare earth phosphate and its five principle single-component xenotime $REPO_4$ with different REEs (Sc, Lu, Yb, Er, and Y) were explored as potential EBCs. The selection or combination of different REEs with various ionic radii from larger Y^{3+} to smaller Sc^{3+} allows the maintenance of the xenotime framework while enhancing structural resilience through structural distortion. In addition, high-entropy materials, a new class of materials composed of five or more elements in nearly equal proportions [25,27–29], display a "cocktail effect", where interactions between elements result in unique material characteristics [30,31]. High-entropy components are expected to possess desirable properties for EBC applications, including enhanced thermal stability, mechanical strength, low thermal conductivity, a slow grain growth rate, and resistance to CMAS corrosion [31–34]. High-entropy phosphate and single-component $REPO_4$ were synthesized via chemical coprecipitation and consolidated into dense pellets via spark plasma sintering (SPS) techniques. The samples were characterized via X-ray diffraction (XRD), scanning electron microscopy (SEM), and thermogravimetric analysis (TGA) to determine their phase, microstructure, and phase stability, respectively. The temperature dependence of the CTEs and thermal diffusivity/conductivity were investigated via dilatometry and laser flash analysis (LFA) techniques, respectively. CMAS corrosion was tested at 1300 °C for 5, 45, and 96 h, and the corroded samples were characterized via XRD and SEM to identify new phases and microstructure variations. The effects of the ionic radius of the RE on the CTE, thermal conductivity, and reaction kinetics were systematically studied. The main objective of this work is to elucidate the effects of critical material parameters (such as ionic radius, ionic mass, and structural disordering) of REEs on the thermal properties (CTEs and thermal conductivity) and CMAS corrosion (reaction layer thickness). Insights gained from this study on the correlations among the composition, structure, and properties and the critical materials governing their thermal and corrosion performance can be leveraged for developing new xenotime $REPO_4$ materials as potential EBCs for SiC–CMCs.

2 Experimental

2.1 $REPO_4$ and HE$(5RE_{0.2})PO_4$ synthesis

Single-component $REPO_4$ and HE $(5RE_{0.2})PO_4$ xenotime rare earth phosphates were synthesized via a chemical coprecipitation route using 99.99% pure RE_2O_3 (RE = Sc, Lu, Yb, Er, and Y) (Alfa Aesar, USA) as the raw materials. For $(5RE_{0.2})PO_4$ synthesis, the oxide powders were mixed well according to the stoichiometric ratio and ball milled via a high-energy ball mill (FRITSCH-pulverizette 7, Fritsch GmbH, Germany) for 24 h at 500 r·min^{-1}. Single and HE rare earth phosphates were synthesized separately. The oxide powders were mixed in a glass beaker with deionized (DI) water, and then 70 wt% HNO_3 was added to the mixture. After the reaction, when $RE(NO_3)_3$ formed, 85 wt% H_3PO_4 was slowly added to the mixture. The chemical reactions proceed as Reactions (2) and (3):

$$RE_2O_3(s) + 6HNO_3(l) \rightarrow 2RE(NO_3)_3(aq) + 3H_2O(l) \quad (2)$$

$$RE(NO_3)_3(aq) + H_3PO_4(l) \rightarrow REPO_4(aq) + 3HNO_3(l) \quad (3)$$

To obtain a homogeneous solution of $RE(NO_3)$, the mixture was stirred via magnetic stirring at 400 °C for 5 h. After that, an excess amount of H_3PO_4 was added to reduce $RE(NO_3)_3$ to $REPO_4$. The mixture was stirred for one more hour to prepare a homogeneous mixture, and then, the precipitated powders were filtered via filter paper. The filtered powders were rinsed multiple times with DI water. Finally, the collected powders were dried overnight at 90 °C, crushed via a mortar and pestle set, and calcined in a box furnace in open air at 1000 °C overnight.

2.2 $REPO_4$ and HE $(5RE_{0.2})PO_4$ sintering

All single-component $REPO_4$ and $(5RE_{0.2})PO_4$ pellets were sintered via an SPS system (Model 10-3 SPS, Thermal Tech. LLC, CA) at a temperature of 1500 °C. One gram of $REPO_4$ powders was loaded in a graphite die, and 0.2 mm thick graphite paper was used between the powders and dies to act as a physical barrier. The sintering process used a heating rate of 200 °C·min^{-1} up to 1500 °C in an Ar environment, with 5 min hold time under a pressure of 50 MPa. Finally, the sintered pellets were polished with silicon carbide abrasive papers, followed by a colloidal silica suspension. These pellets were calcined at 1300 °C overnight to remove the graphite from the pellet before the CTE and thermal diffusivity/conductivity measurements, as well as CMAS corrosion tests.

2.3 Phase, thermal stability, and thermal property characterizations of $REPO_4$ and HE $(5RE_{0.2})PO_4$

The phase and phase stability of all the single and $(5RE_{0.2})PO_4$ rare earth phosphates were confirmed via a powder X-ray diffractometer (Panalytical X′ Pert Pro system, Westborough, USA) and a thermogravimetric analyzer (STA 449 F3 Jupiter, NETZSCH, Germany), respectively. The phase stability measurement was carried out in an Ar environment, and approximately 30 mg of powders were loaded in an alumina crucible and heated from room temperature to 1300 °C at a heating rate of 10 °C·min^{-1}. The CTE and thermal diffusivity of the

consolidated SPS pellets were measured via a thermal dilatometer (DIL 402 Expedis Supreme, NETZCH, Germany) and a laser flash apparatus (LFA-457, NETZCH, Germany) in an Ar environment, respectively. For the CTE measurements, pellets of 13 mm in diameter were trimmed 1 mm from both edges, polished, and then heated from 200 to 1300 °C at a heating rate of 10 °C·min^{-1}. Prior to conducting the thermal diffusivity measurements, the front and back surfaces of the $REPO_4$ pellets were coated with thin layers of graphite to reduce radiative heat transfer through the pellets. The Cape-Lehmann method, which is based on a nonlinear regression model, was used to determine the thermal diffusivity [35]. The specific heat of the $REPO_4$ samples was taken from Refs. [36–40], and for the $(5RE_{0.2})PO_4$ phosphates, the specific heat was calculated according to the mixing rule. The density of the SPS-sintered pellets was measured with distilled water as an immersion medium on the basis of the Archimedes method via an Adam analytical scale (Danbury, USA). The thermal conductivity of all these pellets was calculated via Eq. (4) [35]:

$$k = \alpha \rho c_p \tag{4}$$

where k is the thermal conductivity, α is the thermal diffusivity, ρ is the density, and c_p represents the heat capacity of the sample.

2.4 CMAS synthesis and corrosion experiments

A model composition of $33CaO–9MgO–13AlO_{1.5}–45SiO_2$ ($C_{33}M_9Al_{13}S_{45}$) CMAS was used in this work, which is the same as that used in previous studies [20,22,23, 26]. In accordance with the stoichiometric ratio, high-purity oxides such as CaO, MgO, Al_2O_3, and SiO_2 (99.9%, Alfa Aesar, USA) were used as starting materials for CMAS glass synthesis. The mixture was subsequently heated to 1300 °C and maintained at this temperature for 8 h in a platinum crucible. Finally, the mixture was quenched in water to produce CMAS glass, which was ground to superfine powders via a mortar and pestle set for the CMAS corrosion tests.

The CMAS corrosion tests were performed at 1300 °C for 5, 45, and 96 h. The samples were subsequently characterized via optical microscopy, SEM, and XRD to understand their morphology, microstructure, and phase formation. Thirty milligrams of CMAS powders were placed on the top of a 10 mm diameter $REPO_4$ pellet, and a drop of ethyl alcohol was added to keep the powders on the polished surface of the $REPO_4$ pellet. The samples with CMAS were then heated to a maximum exposure temperature of 1300 °C at a heating rate of 5 °C·min^{-1} in an open-air box furnace and held for 5, 45, and 96 h. The CMAS-corroded samples were cut along the diameter, polished with SiC sandpaper and a colloidal silica suspension, and then examined by backscattering SEM to observe the microstructure, CMAS penetration, and reaction layer thickness. The phase compositions in the reaction layer and residual CMAS, as well as below the reaction layer, were identified via an energy-dispersive X-ray spectroscope (EDS; X-Max 80, Oxford Instruments, UK).

3 Results and discussion

3.1 XRD and TGA analysis

The XRD patterns of the SPS-sintered $REPO_4$ (RE = Sc, Lu, Yb, Er, and Y) pellets are shown in Fig. 1(a). The XRD patterns of the five single-component phosphates are similar; however, the peak positions are not identical because of the different ionic radii of the RE elements. The XRD patterns of $REPO_4$ match the standard XRD patterns of $LuPO_4$ (JCPDS No. 01-077-8389) and $ScPO_4$ (JCPDS No. 00-008-0047), indicating the formation of the same crystal structure (xenotime phase) for all these $REPO_4$ samples. A close-up view of the XRD patterns (within the 2θ range from 25° to 28°) is shown in Fig. 1(b) to observe the effect of the ionic radius of RE elements. The ionic radii of Sc^{3+}, Lu^{3+}, Yb^{3+}, Er^{3+}, and Y^{3+} in the 8-fold coordination are shown in Table 1. As the ionic radius of RE increases (from Sc to Y), there is a corresponding shift in the diffraction peaks to lower angles. Among all these RE elements, the ionic size of Sc^{3+} is much smaller than that of Lu, Yb, Er, and Y. Consequently, the XRD pattern of $ScPO_4$ exhibits a distinctive diffraction peak shift toward the highest 2θ angles, setting it apart from the XRD patterns of the remaining four RE phosphates [41]. The XRD patterns of $(5RE_{0.2})PO_4$ powders and the reference patterns of the five single-component phosphates $REPO_4$ (RE = Sc, Lu, Yb, Er, and Y) are shown in Fig. 1(c). This indicates pure xenotime phase formation in $(5RE_{0.2})PO_4$, and its XRD peaks lie in the middle of those of the five $REPO_4$ samples (RE = Sc, Lu, Yb, Er, and Y), which coincide with those of $LuPO_4$ (PDF#43-0003). Additionally, the FullProf Suite (version 7.40-Jan2021-ILL JRC) software was used for Rietveld refinement to identify detailed information regarding the lattice parameters of $(5RE_{0.2})PO_4$, and the refined result is displayed inFig. 1(d). The calculated and corrected diffraction patterns show minimal deviation (R_p = 2.20%, and R_{wp} = 3.53%) from the experimental XRD pattern, indicating that the adjusted structural model is reliable. The lattice parameters of $(5RE_{0.2})PO_4$ are $a = b = 6.82$ Å and $c = 5.97$ Å, and according to the refined cell dimension, the theoretical density of $(5RE_{0.2})PO_4$ is shown in Table 1. Figure 1(e) shows the SEM image and corresponding EDS mappings of the SPS-sintered pellets of $(5RE_{0.2})PO_4$. There are no cracks or large pores present in the sample. The EDS mappings show the presence of all the RE elements (RE = Sc, Lu, Yb, Er, and Y) homogeneously in $(5RE_{0.2})PO_4$, and there are no signs of elemental segregation. These results indicate the formation of a single solid solution phase in the high-entropy phosphate.

The TGA curves of $REPO_4$ and $(5RE_{0.2})PO_4$ (RE = Sc, Lu, Yb, Er, and Y) powders in Fig. 2 show no appreciable weight loss when heated to 1200 °C, and only a negligible mass change (< 1.0 wt%) is observed at 1300 °C. These results imply that, in general, all six rare earth phosphates have good thermal stability in this temperature range. Compared with the other samples, the $ScPO_4$ and $LuPO_4$ samples have slightly better thermal stability, with greater mass loss (< 0.6%). The overall minimal mass loss suggests that rare-earth (RE) phosphates are highly thermally stable, making them suitable for high-temperature applications.

3.2 Thermal properties of $REPO_4$ and HE $(5RE_{0.2})PO_4$

High-temperature thermal properties such as the CTE and thermal diffusivity/conductivity are crucial for EBC applications. Figures 3(a) and 3(b) illustrate the linear expansion rates and corresponding CTEs of $REPO_4$ and $(5RE_{0.2})PO_4$ (RE = Sc, Lu, Yb, Er, and Y) pellets in the temperature range from 200 °C to 1300 °C, respectively. Lu^{3+}, Yb^{3+}, Er^{3+}, and Y^{3+} cations have similar ionic radii, and their measured CTE values are close to each other. The measured CTEs of $REPO_4$ (RE = Lu, Yb, Er, and Y) are comparable to previously reported values ($LuPO_4$ (5.92×10^{-6} °C^{-1})) and $YbPO_4$ (6.0×10^{-6} °C^{-1}) of xenotime rare earth phosphates [22,23]. Among the single-component systems studied here, $ScPO_4$, which has the smallest ionic radius and atomic mass of Sc^{3+}, has a higher CTE value than the other systems in the same temperature range. The ionic mass, radius, and average CTE values of these rare earth phosphates in the temperature range from 200 to 1300 °C are shown in Table 1. The variations in the average CTE values in the temperature range of 200–1300 °C with

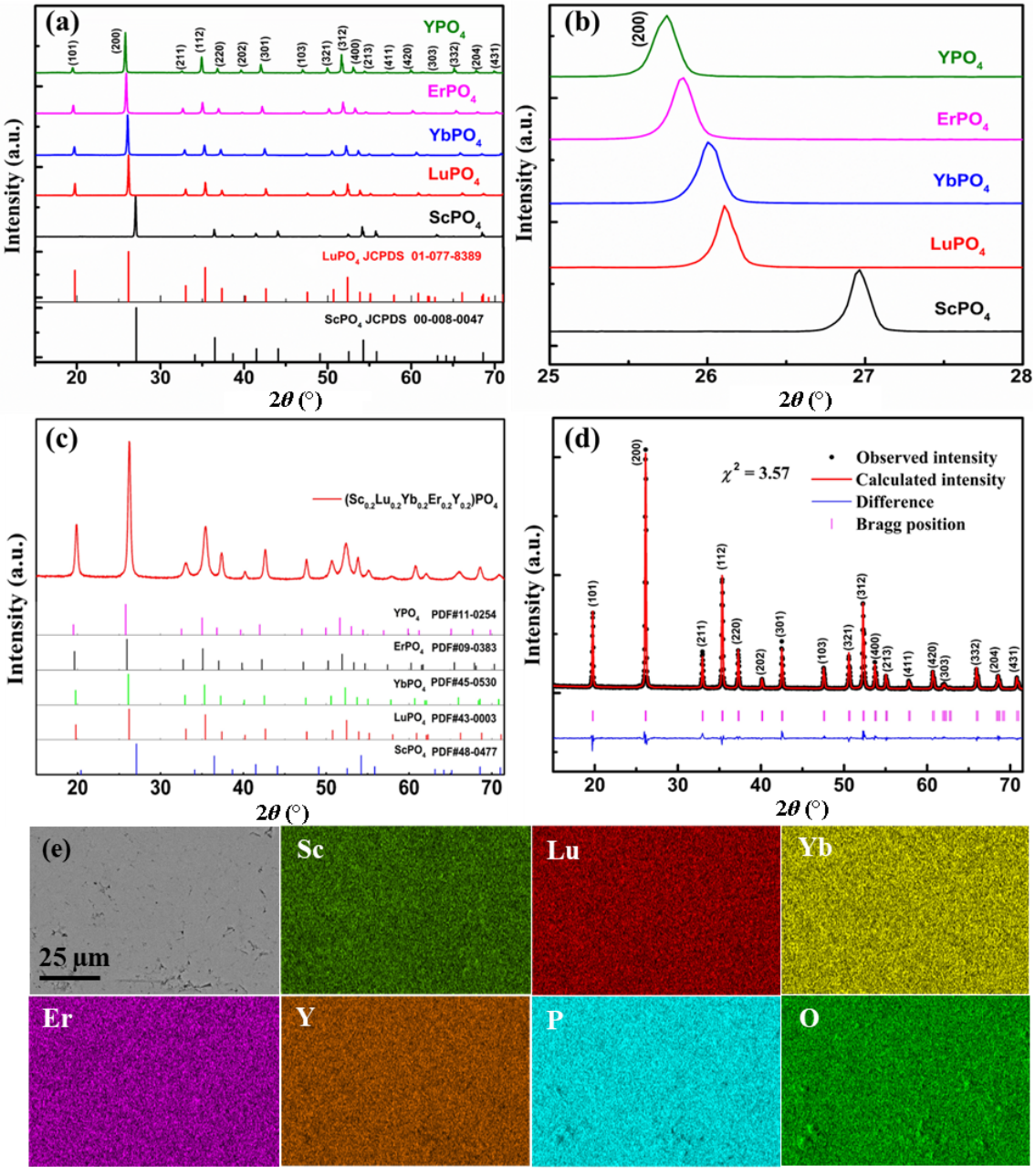

Fig. 1 (a) XRD patterns of $REPO_4$ (RE = Sc, Lu, Yb, Er, and Y) pellets after SPS sintering. (b) XRD patterns of $REPO_4$ (RE = Sc, Lu, Yb, Er, and Y) in 2θ range of 25°–28°. (c) XRD patterns of $(5RE_{0.2})PO_4$ powders and reference patterns. (d) Rietveld refinement of XRD patterns for $(5RE_{0.2})PO_4$. (e) SEM images and corresponding EDS mappings of $(5RE_{0.2})PO_4$ pellet.

Table 1 Ionic mass, ionic radius, average CTE, experimental, theoretical, and relative density values of $REPO_4$ and HE $(5RE_{0.2})PO_4$ (RE = Sc, Lu, Yb, Er, and Y)

Rear earth phosphate	Ionic mass of rare earth elements	Ionic radius rare earth elements (pm)	Average CTE (°C^{-1}) (200–1300 °C)	Measured density (g/cm^3)	Theoretical density (g/cm^3)	Relative density (%)
$ScPO_4$	44.95	87.0	6.98×10^{-6}	3.63±0.03	3.69	98.4
$LuPO_4$	174.97	97.7	5.69×10^{-6}	6.42±0.03	6.53	98.3
$YbPO_4$	173.04	98.5	5.98×10^{-6}	6.37±0.04	6.52	97.7
$ErPO_4$	167.26	100.4	5.59×10^{-6}	5.95±0.03	6.06	98.2
YPO_4	88.90	101.9	5.70×10^{-6}	4.20±0.04	4.27	98.4
HE$(5RE_{0.2})PO_4$	129.80	97.1	6.39×10^{-6}	5.23±0.04	5.37	97.4

the ionic mass and radius are plotted in Figs. 3(c) and 3(d), respectively. The average CTE is better correlated with the ionic radius than with the ionic mass. Specifically, the CTE value of RE phosphates decreases with increasing ionic radius of rare earth elements (REEs). This is similar to what was observed in monazite $REPO_4$, where a shorter atomic bond length results in a greater asymmetry of the interatomic potential and, thus, a higher CTE [42].

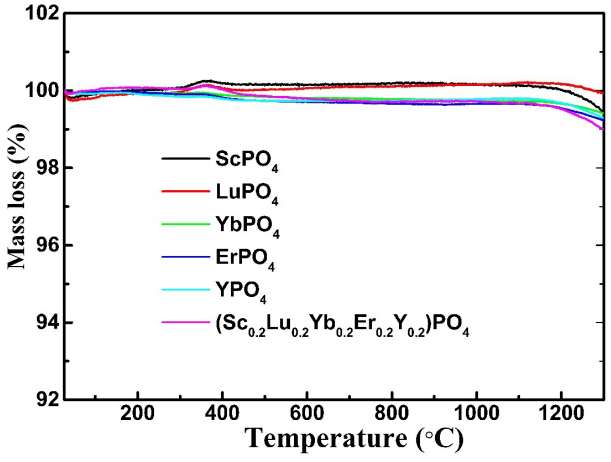

Fig. 2 TGA curves of $REPO_4$ (RE = Sc, Lu, Yb, Er, and Y) and $(5RE_{0.2})PO_4$ powders from room temperature to 1300 °C.

The average CTE values of $REPO_4$ (RE = Lu, Yb, Er, and Y) are in the range of (5.59–5.98)×10^{-6} $°C^{-1}$, which are close to those of SiC–CMCs ((4.5–5.5)×10^{-6} $°C^{-1}$) [8]. The small difference in the CTE between $REPO_4$ (RE = Lu, Yb, Er, and Y) and SiC–CMCs can reduce the residual stress between the ceramic coating and the substrate [1,9], making them suitable candidates as topcoat materials for EBC applications to protect SiC–CMCs. However, $ScPO_4$ has a higher average value of CTE (6.98×10^{-6} $°C^{-1}$). The high entropy $(5RE_{0.2})PO_4$ has an average CTE of 6.39×10^{-6} $°C^{-1}$, which lies between the CTE values of $ScPO_4$ and that of the other four $REPO_4$ (where RE = Lu, Yb, Er, and Y). These results imply that the incorporation of smaller Sc^{3+} ions into the phosphate likely increases the CTE, and thus, to design high-entropy phosphates with lower CTE values (less than 6×10^{-6} $°C^{-1}$), it is necessary to exclude Sc.

The temperature-dependent thermal diffusivity and conductivity of the SPS-sintered $REPO_4$ and $(5RE_{0.2})PO_4$ (RE = Sc, Lu, Yb, Er, and Y) pellets are shown in Figs. 4(a) and 4(c), respectively. Figure 4(b) shows the specific heat of single component $REPO_4$, taken from Refs. [36–40]. In ceramic materials, the thermal diffusivity/conductivity decreases steadily with increasing temperature due to the predominant phonon–phonon Umklapp scattering [43]. In this study, the thermal diffusivity monotonically decreases with increasing temperature, as shown in Fig. 4(a), reaching values of ~1 $mm·s^{-2}$ at 1000 °C for heavier elements such as Lu, Yb, Er, and $(5RE_{0.2})PO_4$. The thermal conductivity values are corrected for porosities in the samples. Figure 4(d) shows that the thermal conductivity (at 1273 K) decreases with increasing atomic mass of the rare earth elements. Among all the $REPO_4$ samples studied in this work, those with heavy elements such as Lu, Yb, and Er exhibit relatively low thermal conductivities across the temperature range, and at 1273 K, their values are 3.15, 3.14, and 3.03 $W·m^{-1}·K^{-1}$ for $LuPO_4$, $YbPO_4$, and $ErPO_4$, respectively, and relatively high thermal conductivities for lighter elements (at 1273 K, 5.6 $W·m^{-1}·K^{-1}$ for $ScPO_4$ and 3.8 $W·m^{-1}·K^{-1}$ for YPO_4). Additionally, owing to the size and mass disorder within the system, $(5RE_{0.2})PO_4$ has the lowest thermal conductivity compared with all single-component $REPO_4$ [33]. Recently, Hu *et al.* [23] reported that the thermal conductivity of $LuPO_4$ at 1273 K was 2.2 $W·m^{-1}·K^{-1}$. They prepared samples using different chemicals, which could be the reason for the different thermal conductivity values of $LuPO_4$. It was also observed that the thermal conductivity/phonon scattering of RE phosphates depends upon lattice distortion, which increases as the difference in the atomic masses of the

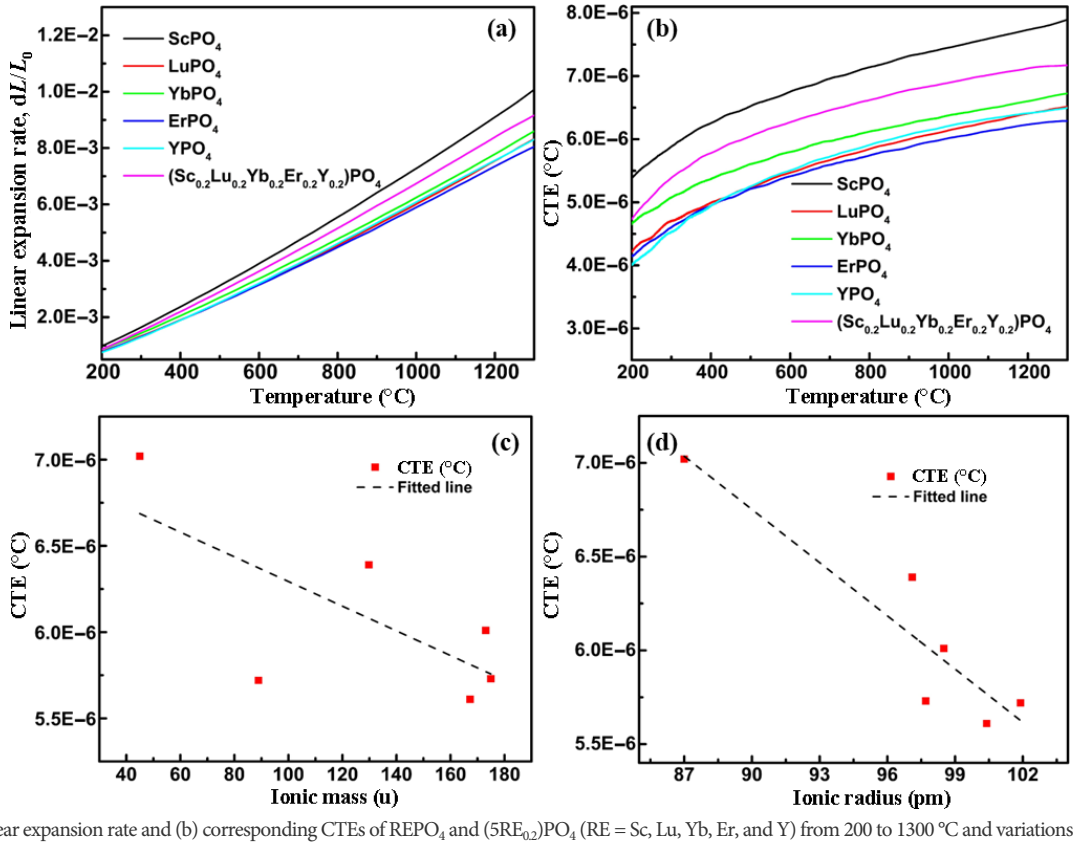

Fig. 3 (a) Linear expansion rate and (b) corresponding CTEs of $REPO_4$ and $(5RE_{0.2})PO_4$ (RE = Sc, Lu, Yb, Er, and Y) from 200 to 1300 °C and variations in average CTE values in temperature range of 200–1300 °C with (c) ionic mass and (d) ionic radius of rare earth elements. CTE data for $LuPO_4$ were taken from Ref. [26].

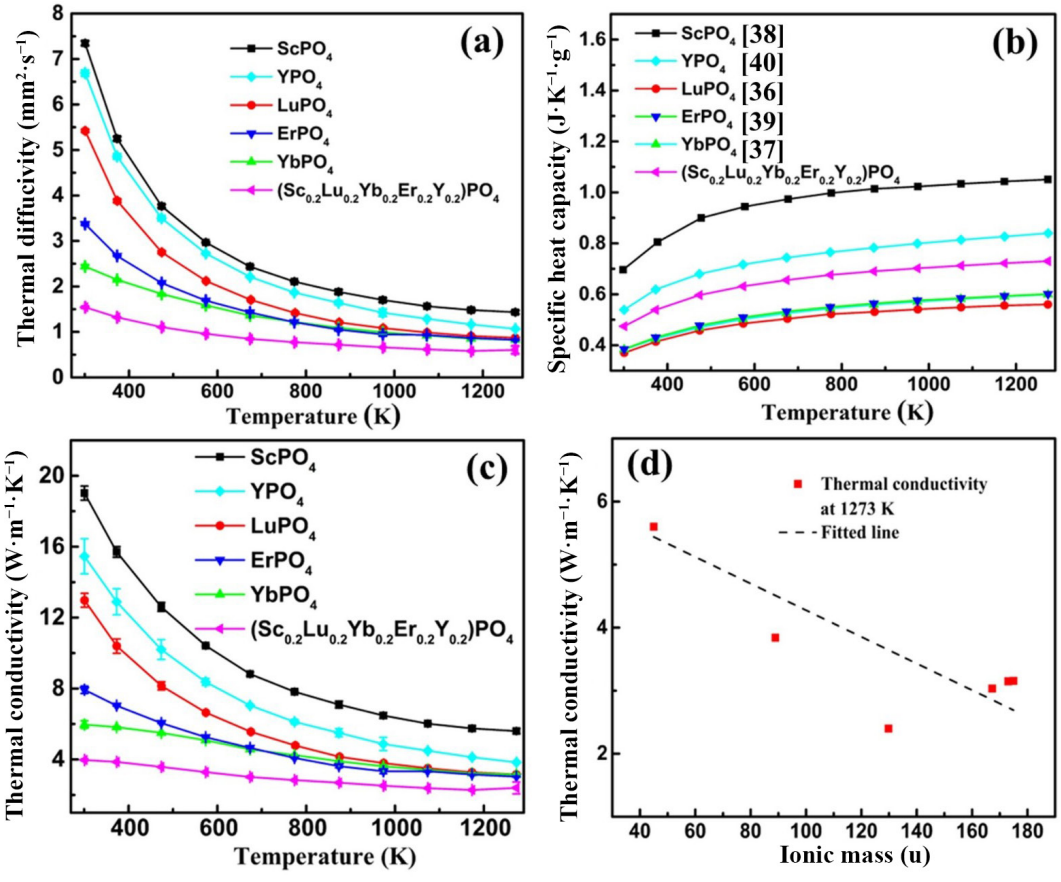

Fig. 4 (a) Thermal diffusivity, (b) specific heat capacity (taken from Refs. [36–40]), (c) thermal conductivity of $REPO_4$ and $(5RE_{0.2})PO_4$ (RE = Sc, Lu, Yb, Er, and Y) pellets from room temperature to 1273 K, and (d) variation in thermal conductivity (at 1273 K) with the ionic mass of rare earth elements. Thermal conductivity data of $LuPO_4$ were taken from Ref. [26].

components increases [41]. In single-component $REPO_4$, the average atomic mass of PO_4 remains constant, whereas the atomic mass of RE ions gradually increases from Sc to Lu (Table 1). Consequently, the difference in the atomic masses of the components increases, leading to increased phonon scattering and decreased thermal conductivity [44]. Thus, relatively low thermal conductivities are observed in heavier $REPO_4$ (i.e., $LuPO_4$, $YbPO_4$, and $ErPO_4$) throughout the temperature range. Experimentally, the greater Young's modulus of xenotime RE phosphates with smaller RE^{3+} radii (such as Sc and Y) indicates stronger bonds, which enhances phonon transport and thermal conductivity [45]. The Young's modulus values for YPO_4 (224.1 GPa) and $ScPO_4$ (210.8 GPa) are the highest and second highest among these RE phosphates [41]; thus, they have higher thermal conductivities than other RE phosphates (RE = Lu, Yb, and Er).

The thermal conductivity of ceramic materials can be tuned by creating defects and disorder in multicomponent/HE systems [25,43]. Compared with single-component $REPO_4$ (RE = Sc, Lu, Yb, Er, and Y), HE $(5RE_{0.2})PO_4$ has the lowest thermal conductivity from room temperature to 1273 K, indicating its great potential for thermal insulation among all these materials. XRD and SEM analyses revealed that RE atoms (Sc > Y) were successfully incorporated into $(5RE_{0.2})PO_4$. Point defects and lattice distortions are induced during the formation of the single-phase solid solution because of the size and mass difference in RE atoms. Therefore, the defect concentration in $(5RE_{0.2})PO_4$ is expected to be greater than that in single-component RE phosphates, leading to increased phonon scattering and a lower thermal conductivity [44,46]. The low thermal conductivity is beneficial for reducing the surface temperature of a gas turbine engine in EBC applications. The low thermal conductivity of HE $REPO_4$ is consistent with previously published results for HE ceramic materials [27,33,34,43].

3.3 $REPO_4$/HE$(5RE_{0.2})PO_4$-CMAS interaction at 1300 °C

Figures 5(a)–5(c) show the $REPO_4$ and $(5RE_{0.2})PO_4$ pellets after exposure to the CMAS reaction at 1300 °C for 5, 45, and 96 h, respectively. These optical images indicate the presence of residual CMAS after the corrosion test at 1300 °C, and multiple cracks were observed in the residual CMAS during cooling. The cross-sectional view of these pellets was analyzed via SEM in the following sections.

X-ray diffraction was performed to identify the phase and crystal structure of the CMAS corroded $REPO_4$ pellets. Figures 6–8 show the XRD patterns of the surface of $REPO_4$ (RE = Sc, Lu, Yb, Er, and Y) after the CMAS attack at 1300 °C for 5, 45, and 96 h, respectively. The reference pattern for $LuPO_4$ in Figs. 6–9 corresponds to the xenotime phase, which is consistent with other $REPO_4$ compounds (RE = Sc, Yb, Er, and Y). Thus, we retain the $LuPO_4$ reference pattern in Figs. 6–8. XRD results indicate that additional diffraction peaks are present alongside the $REPO_4$ peaks, suggesting that a reaction occurs between $REPO_4$ and CMAS at 1300 °C. These extra peaks match those of the $Ca_8MgRE(PO_4)_7$ phase, and the reference pattern of a similar phase, $Ca_8MgLu(PO_4)_7$, is shown in Fig. 6. The peak intensity of this phase does not precisely match that of the reference pattern, likely because of the preferred growth direction of the new phase [22]. Compared with the corrosion behavior of the four $REPO_4$

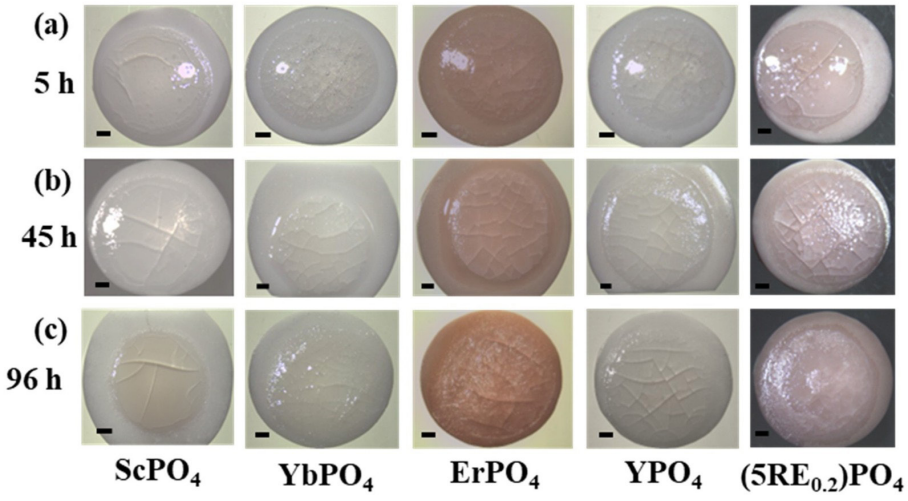

Fig. 5 Optical images of $REPO_4$ (RE = Sc, Yb, Er, and Y) and $(5RE_{0.2})PO_4$ (RE = Sc, Lu, Yb, Er, and Y) pellets after CMAS reaction at 1300 °C for (a) 5, (b) 45, and (c) 96 h. The scale bar is 1 mm for all optical images. The optical images of $LuPO_4$ can be found in our prior work in Ref. [26].

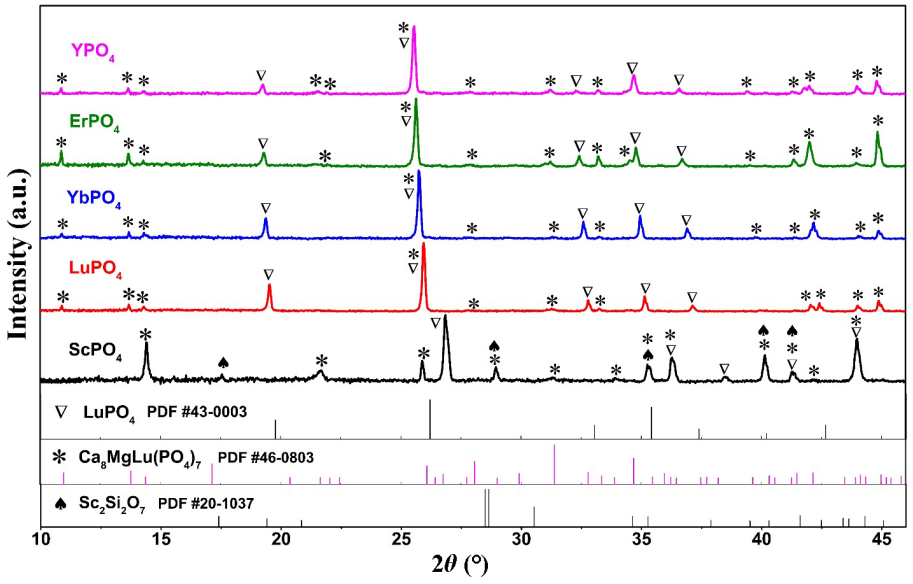

Fig. 6 XRD patterns of $REPO_4$ (RE = Sc, Lu, Yb, Er, and Y) surface after CMAS reaction for 5 h at 1300 °C. XRD data of $LuPO_4$ taken from Ref. [26].

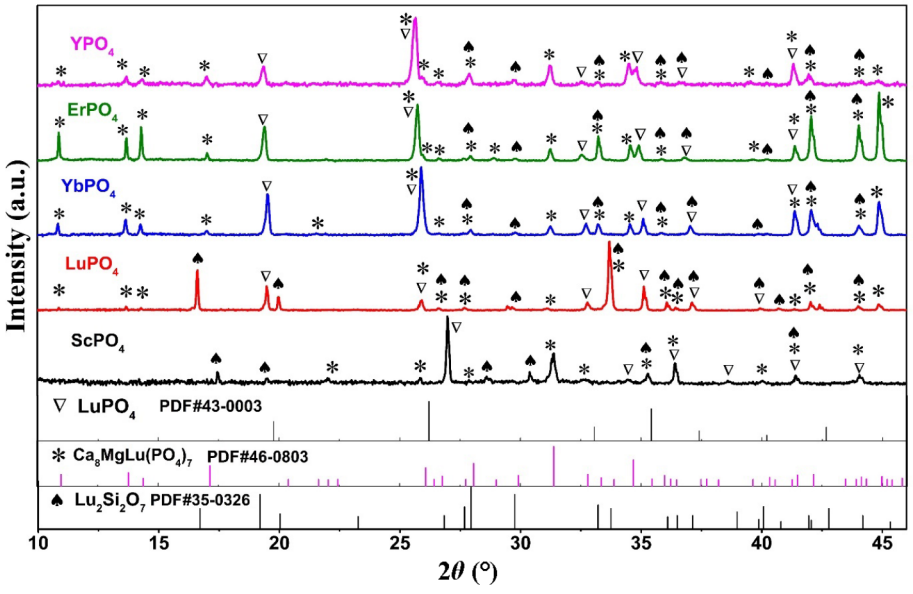

Fig. 7 XRD patterns of $REPO_4$ (RE = Sc, Lu, Yb, Er, and Y) surface after CMAS reaction for 45 h at 1300 °C. XRD data of $LuPO_4$ taken from Ref. [26].

(RE = Lu, Yb, Er, and Y) phosphates, $ScPO_4$ has an additional disilicate phase, $Sc_2Si_2O_7$, along with the common phase of $Ca_8MgRE(PO_4)_7$. This indicates that owing to the smaller ionic radius of Sc, $ScPO_4$ reacts differently with molten CMAS at 1300 °C than the other four $REPO_4$ samples do (RE = Lu, Yb, Er, and Y). The disilicate phase probably formed due to the faster reaction of $ScPO_4$ with SiO_2. This result implies a greater thermodynamic driving force because of the greater negative Gibbs free energy for the reaction between $ScPO_4$ and SiO_2, making it more spontaneous under similar conditions.

To investigate the effect of prolonged corrosion time on the reaction products of $REPO_4$ (RE = Sc, Lu, Yb, Er, and Y), XRD was also performed on the 45- and 96-h corroded samples. With increasing corrosion time, more diffraction peaks were observed in all $REPO_4$ samples. The XRD results after 45 and 96 h of corrosion revealed the presence of two typical phases, i.e., $Ca_8MgRE(PO_4)_7$ and disilicate $RE_2Si_2O_7$, and PDF curves of $Ca_8MgLu(PO_4)_7$ and $Lu_2Si_2O_7$ are shown in Figs. 7 and 8. With prolonged duration, disilicate ($RE_2Si_2O_7$) peaks emerge, and their intensity increases with CMAS reaction time. Moreover, the intensity of the pure $REPO_4$ peak decreases in some cases, such as $ErPO_4$ and $LuPO_4$. This suggests that the thickness of the reaction layer increases with prolonged duration. Note that the intensity of the diffraction peaks from corrosion products, such as disilicate and $Ca_8MgRE(PO_4)_7$, varies with different samples, which could be a result of the variation in the residual CMAS on the sample surfaces.

Figure 9 shows the XRD patterns of the surface of HE $(5RE_{0.2})PO_4$ after the CMAS reaction for 5, 45, and 96 h at 1300 °C and the reference patterns of $Ca_8MgLu(PO_4)_7$ and $Lu_2Si_2O_7$. The reaction products of the $(5RE_{0.2})PO_4$–CMAS interaction revealed the presence of $Ca_8MgRE(PO_4)_7$ for all three exposure durations. Prolonged exposure (45 and 96 h) revealed the formation of the disilicate phase ($RE_2Si_2O_7$), similar to that observed in the interactions of the five single elements $REPO_4$ (RE = Sc, Lu, Yb, Er, and Y) with CMAS. Similarly, after the $(5RE_{0.2})PO_4$–CMAS interaction, $REPO_4$ peaks can still be observed in the corroded samples for all three durations, and their intensity decreases with increasing reaction time.

To investigate the microstructure, reaction layer thickness, and

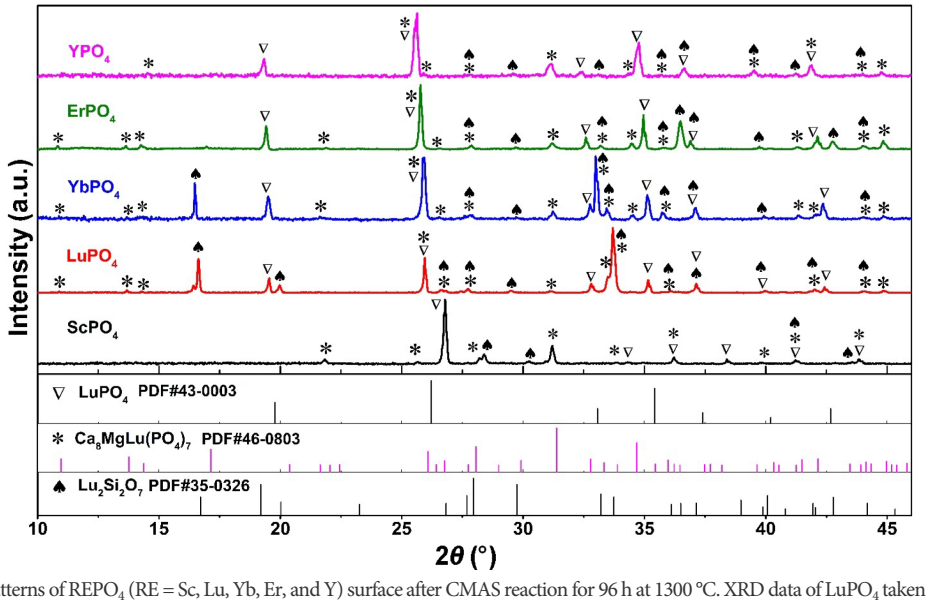

Fig. 8 XRD patterns of $REPO_4$ (RE = Sc, Lu, Yb, Er, and Y) surface after CMAS reaction for 96 h at 1300 °C. XRD data of $LuPO_4$ taken from Ref. [26].

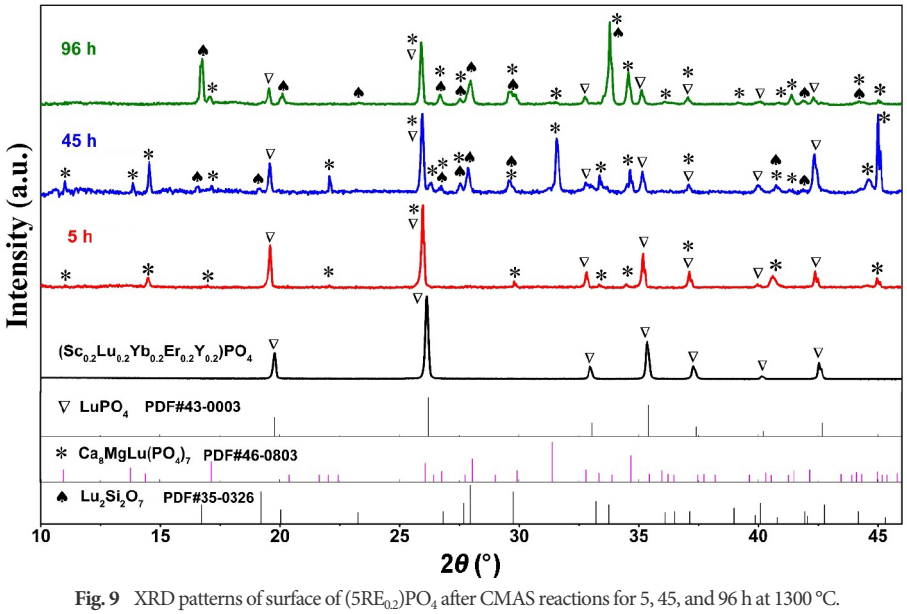

Fig. 9 XRD patterns of surface of $(5RE_{0.2})PO_4$ after CMAS reactions for 5, 45, and 96 h at 1300 °C.

reaction products after CMAS exposure, backscattered electron SEM and EDS maps and line scans were performed on all $REPO_4$ (RE = Sc, Lu, Yb, Er, and Y) and HE $(5RE_{0.2})PO_4$ samples. The melting point of the CMAS used in this study is approximately 1235 °C [23], and the CMAS corrosion test is performed above this temperature. Figures 10–14 show cross-sectional SEM images, EDS mappings, and line scans of three different regions around the $REPO_4$/CMAS interface. In general, all five $REPO_4$ samples formed a continuous, thick, and dense reaction layer after CMAS corrosion for all three durations. There is a significant contrast difference between the residual CMAS, the reaction layer, and the bulk pellet. Furthermore, small contrast differences are observed in the reaction layers of all the $REPO_4$ samples because of the concentration differences in REEs along the depth of the reaction layer. The reaction layer halted CMAS penetration into the bulk matrix, and there was a proportional relationship between the corrosion time and reaction layer thickness at 1300 °C for all $REPO_4$ samples. For comparison, the reaction layer thickness was measured at 20 different positions on the cross-sections of the CMAS corroded samples, and standard deviations were calculated on the basis of those measurements. SEM images show white spots on the reaction layer after 96 h of CMAS corrosion in three $REPO_4$ samples (RE = Lu, Yb, and Er), which are the disilicate phase ($RE_2Si_2O_7$), as shown in XRD patterns. Figures 10(e) and 10(f), 11(e) and 11(f), 12(e) and 12(f), 13(e) and 13(f), and 14(e) and 14(f) show the EDS mappings and line scans of the corroded samples after 5 h, respectively. The line scan traverses three different regions, i.e., the residual CMAS (region 1), the reaction layer (region 2), and the bulk $REPO_4$ (region 3), in all the samples. It is evident that Ca and P are significantly enriched at the bottom of the reaction layer, with their concentrations decreasing closer to the top of the reaction layer. Conversely, Si and REEs have higher concentrations toward the top of the reaction layer, with a decrease in concentration as they approach the bulk pellet (i.e., the bottom of the reaction layer). These observations show that the concentrations of the REEs are not constant throughout the reaction layers in all the samples.

The EDS line scan in Fig. 10(f) shows that in $ScPO_4$, the top of the reaction layer is highly enriched with Sc and Si, and the bottom is enriched with Ca and P, which is different from the other four single-component $REPO_4$ samples. Combined with the XRD data (Fig. 6) and elemental analysis via EDS mapping and line scanning, the two reaction layers can be identified as $Sc_2Si_2O_7$ (top layer) and $Ca_8MgSc(PO_4)_7$ (bottom layer). Sc easily reacts with SiO_2 and forms a disilicate phase sooner than other elements due to the more negative Gibbs free energy of the reaction. The thicknesses of the reaction layer in $ScPO_4$ after 5, 45, and 96 h of CMAS corrosion at 1300 °C were 14.3±2.2, 29.1±3.5, and

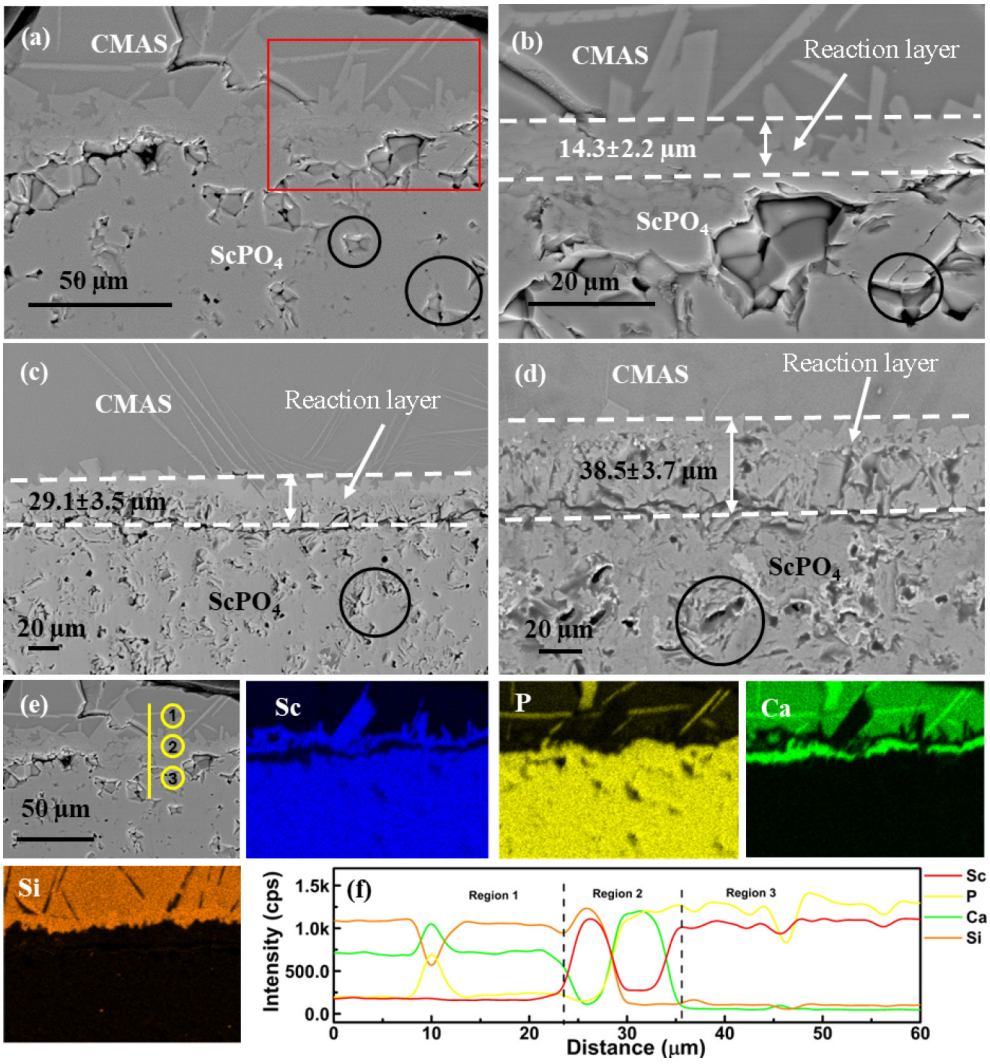

Fig. 10 Backscattered electron SEM images of cross-section of $ScPO_4$ pellet after CMAS reaction at 1300 °C for 5 h: (a) low and (b) high magnification for (c) 45 h and (d) 96 h; (e) EDS mappings of $ScPO_4$ after CMAS reaction for 5 h at 1300 °C; and (f) EDS line scan along yellow line shown in (e).

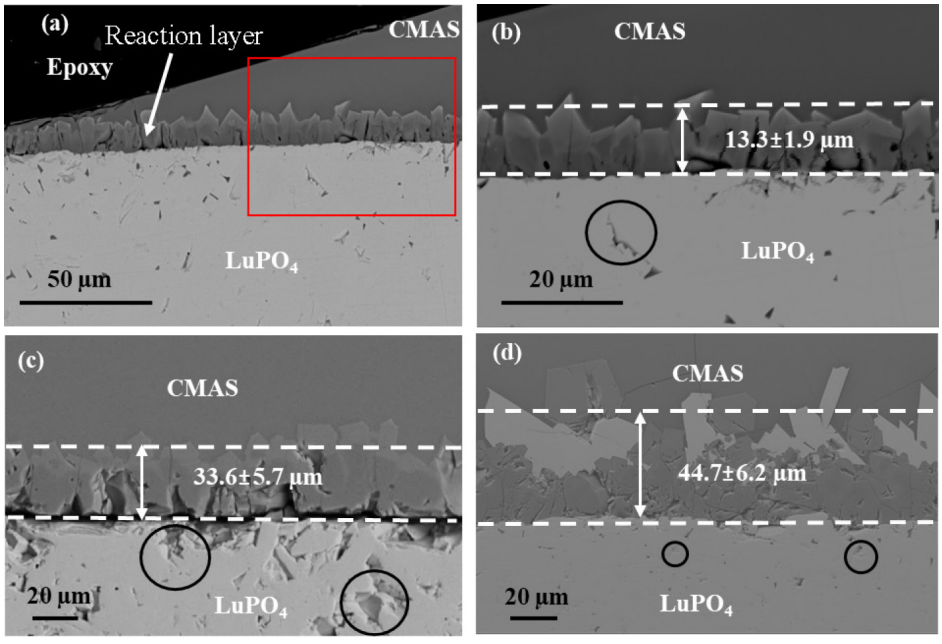

Fig. 11 Backscattered electron SEM images of cross-section of $LuPO_4$ pellet after CMAS reaction at 1300 °C for 5 h at (a) low and (b) high magnification for (c) 45 h and (d) 96 h.

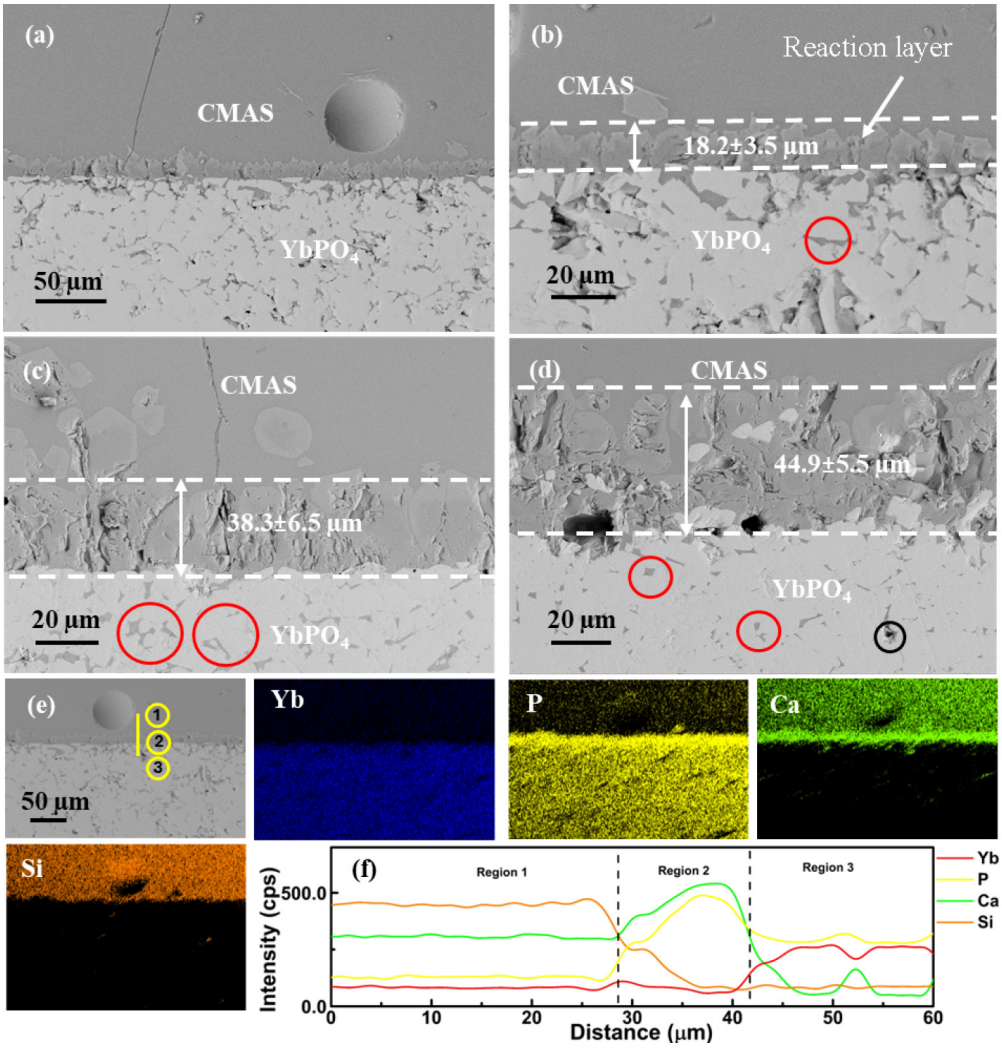

Fig. 12 Backscattered electron SEM images of cross-section of $YbPO_4$ pellet after CMAS reaction at 1300 °C for 5 h. (a) Low- and (b) high-magnification images at (c) 45 h and (d) 96 h. (e) EDS mappings of $YbPO_4$ after CMAS reaction for 5 h at 1300 °C. (f) EDS line scan along yellow lines denoted in (e).

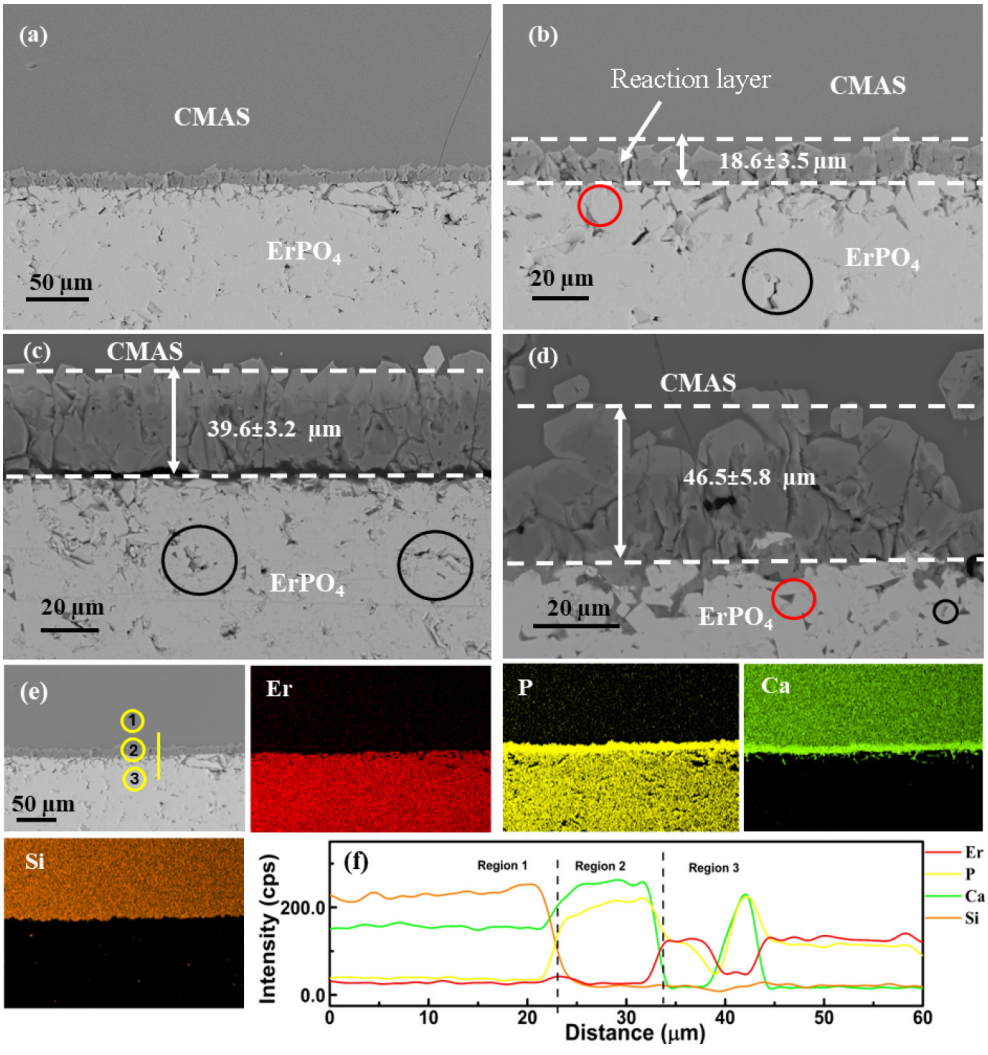

Fig. 13 Backscattered electron SEM images of cross-section of $ErPO_4$ pellet after CMAS reaction at 1300 °C for 5 h: (a) low and (b) high magnification at (c) 45 h and (d) 96 h. (e) EDS mappings of $ErPO_4$ after CMAS reaction for 5 h at 1300 °C. (f) EDS line scan along yellow line denoted in (e).

38.5±3.7 μm, respectively. In addition, the pores marked by black circles beneath the reaction layer are free of CMAS, suggesting that the reaction layer effectively impedes CMAS penetration.

The average thickness of the reaction layer of the $LuPO_4$ samples was approximately 13.3±1.9, 33.6±5.7, and 44.7±6.2 μm after 5, 45, and 96 h of corrosion at 1300 °C, respectively. Similarly, pores beneath the reaction layers devoid of CMAS (identified by black circles in Figs. 11(b)–11(d)) are also identified, indicating the role of the reaction layer in impeding CMAS penetration. The line scan of the three different regions revealed that the reaction layer is highly concentrated with Ca and P, as shown in our previous paper [26]. XRD and EDS analysis confirmed the presence of $Ca_8MgLu(PO_4)_7$ in the reaction layer after 5 h of CMAS testing [26]. SEM analysis of the 96 h CMAS corroded sample revealed the presence of white spots on the reaction layer, which were not observed in the 5- and 45-h CMAS corroded samples and the XRD patterns in Fig. 8 indicate that they were $Lu_2Si_2O_7$ [23].

Similarly, the thickness of the reaction layer increases over time because of corrosion in $YbPO_4$, as shown in Figs. 12(b)–12(d). Under identical experimental conditions, the reaction layer thickness is greater than that of the $ScPO_4$–CMAS and $LuPO_4$–CMAS interactions, indicating a faster formation rate of the interfacial layer in $YbPO_4$. However, CMAS penetrates below the reaction layer for all three durations (shown with red circles in Figs. 12(b)–12(d)), which is not observed in the $ScPO_4$ and $LuPO_4$ samples. In this case, the reaction layer is not dense enough, and some pores are observed in the reaction layer, which could be the reason for CMAS penetration into the bulk $YbPO_4$ pellet. The EDS mapping and line scan over three regions indicate that Ca and P are highly concentrated in the reaction layer, similar to the $LuPO_4$–CMAS interaction.

The average thickness of the reaction layer in $ErPO_4$ was 18.6±3.5, 39.6±3.2, and 46.5±5.8 μm at 5, 45, and 96 h, respectively. The EDS image and line scan, shown in Figs. 13(e) and 13(f), respectively, indicate that Ca and Si do not penetrate below the reaction layer, similar to the observations in the $ScPO_4$ and $LuPO_4$ samples. The dense reaction layer is highly concentrated with Ca and P, similar to the other $REPO_4$ (RE = Lu, Yb). After 96 h of CMAS reaction, a small amount of CMAS is observed below the reaction layer (shown in the red circle) because of the less continuous reaction layer shown in Fig. 13(d).

The YPO_4–CMAS interaction cross-sectional SEM images in Figs. 14(b)–14(d) reveal that the average thicknesses of the reaction layers are 19.4±3.4, 45.3±6.4, and 58.1±7 μm at 5, 45, and 96 h, respectively, and are thicker than those of the other $REPO_4$ layers under the same experimental conditions. The reaction layer is thicker but less homogeneous, i.e., more thickness variations are

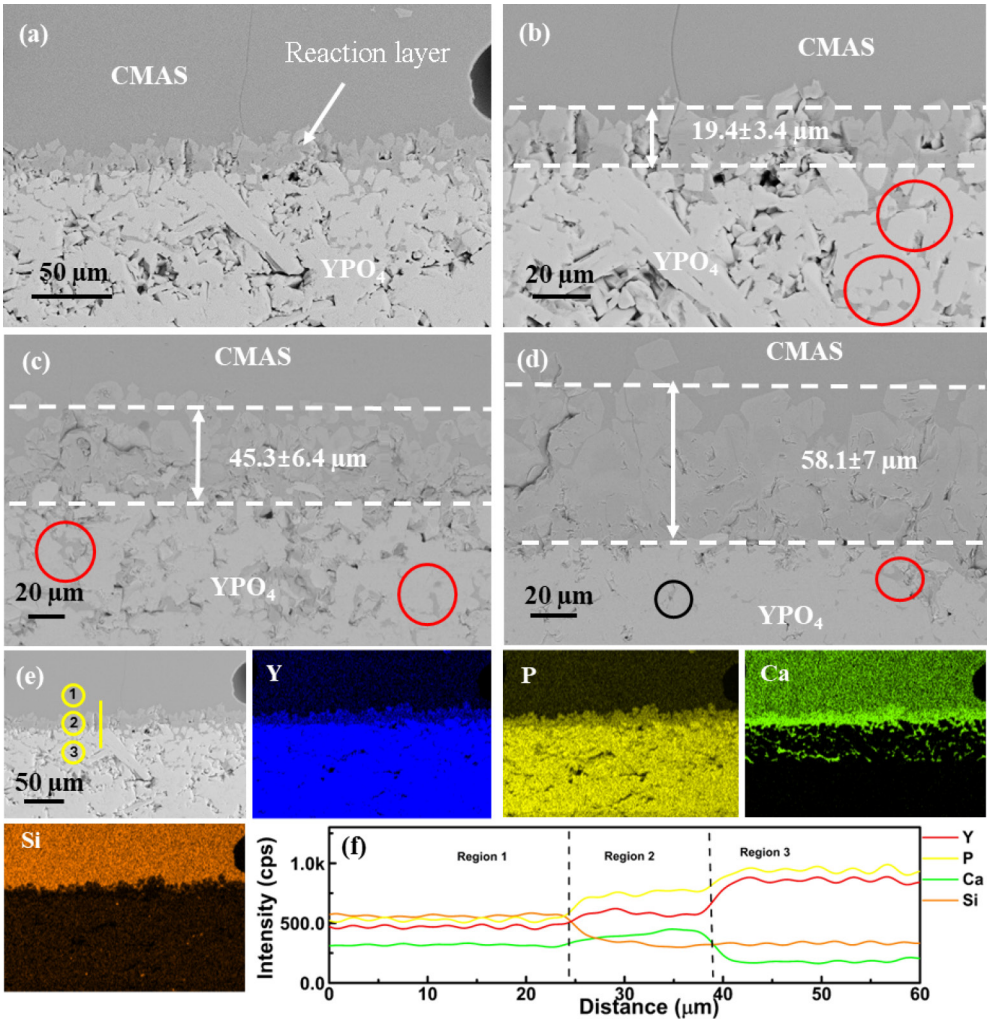

Fig. 14 Backscattered electron SEM images of cross-section of YPO_4 pellet after CMAS reaction at 1300 °C for 5 h. (a) Low- and (b) high-magnification images at (c) 45 h and (d) 96 h. (e) EDS mappings of YPO_4 after CMAS reaction for 5 h at 1300 °C. (f) EDS line scan along yellow line denoted in (e).

observed. Therefore, the Ca penetrates below the reaction layer via grain boundaries up to 60 μm after 5 h of CMAS corrosion. The EDS mappings and line scans in Figs. 14(e) and 14(f) show that the reaction layer contains more REEs, i.e., Y, than the other $REPO_4$ systems do. The P enrichment is moderate in the reaction layer, and a small amount of P is present in the residual CMAS, which is different from other $REPO_4$–CMAS interactions. Owing to the larger ionic radius of Y^{3+}, which results in weaker Y–O bonds than those of smaller rare-earth ions, Y^{3+} can be more easily dissolved into CMAS at higher concentrations than other elements. Owing to the REEs' solubilities in the molten glass and the reaction kinetics for the Ca-enriched interfacial layer, a continuous and dense interfacial layer does not yet form in this particular sample upon CMAS corrosion for 5 h compared with other samples. The 45-h CMAS-corroded sample (Fig. 14(c)) also has a less homogeneous reaction layer, with granules of varying shapes that may be loosely bound, leading to increased CMAS penetration. This study indicates that CMAS penetration depends not only on the thickness but also on the homogeneity (in terms of continuity and fewer pores) of the reaction layer.

CMAS corrosion tests in HE $(5RE_{0.2})PO_4$ were performed under the same experimental conditions. The cross-sectional SEM images of the CMAS corroded HE $(5RE_{0.2})PO_4$ sample in Figs. 15(b)–15(d) show that the average reaction layer thicknesses are 11.1±1.8, 29.5±3, and 36.2±3.9 μm after 5, 45, and 96 h of CMAS exposure, respectively. Compared with that of all the single-component $REPO_4$ samples, the thickness of the reaction layer is the thinnest for all three durations (except for $ScPO_4$ for 45 h). After 5 h of corrosion, the HE $(5RE_{0.2})PO_4$ formed a dense, continuous, homogeneous reaction layer. After 45 h of corrosion, a small amount of CMAS passed through the reaction layer, and CMAS was observed below the reaction layer (marked by a red circle in Fig. 15(c)). After 96 h, CMAS also penetrates below the reaction layer, as marked by the red circles in Fig. 15(d). This could be due to crack formation in the reaction layer. The reaction layer is highly concentrated with Ca and P (Fig. 15(e)). Additionally, the lightweight RE elements Sc and Y are homogeneously distributed in the reaction layer, and the other three heavier RE elements with larger ionic radii are not homogeneously distributed. The line scan in Fig. 15(f) shows that the reaction layer contains high concentrations of Ca and P, similar to the other reaction layers. At the top of the reaction layer, the concentrations of Lu, Yb, and Er are relatively high compared with those at the bottom of the reaction layer. This indicates that the RE element is lighter than the RE element, which is heavier in terms of the composition of the reaction layer.

3.4 Kinetics of interfacial layer formation

The average interfacial layer thickness upon CMAS interaction is summarized in Fig. 16 to determine the reaction kinetics involved

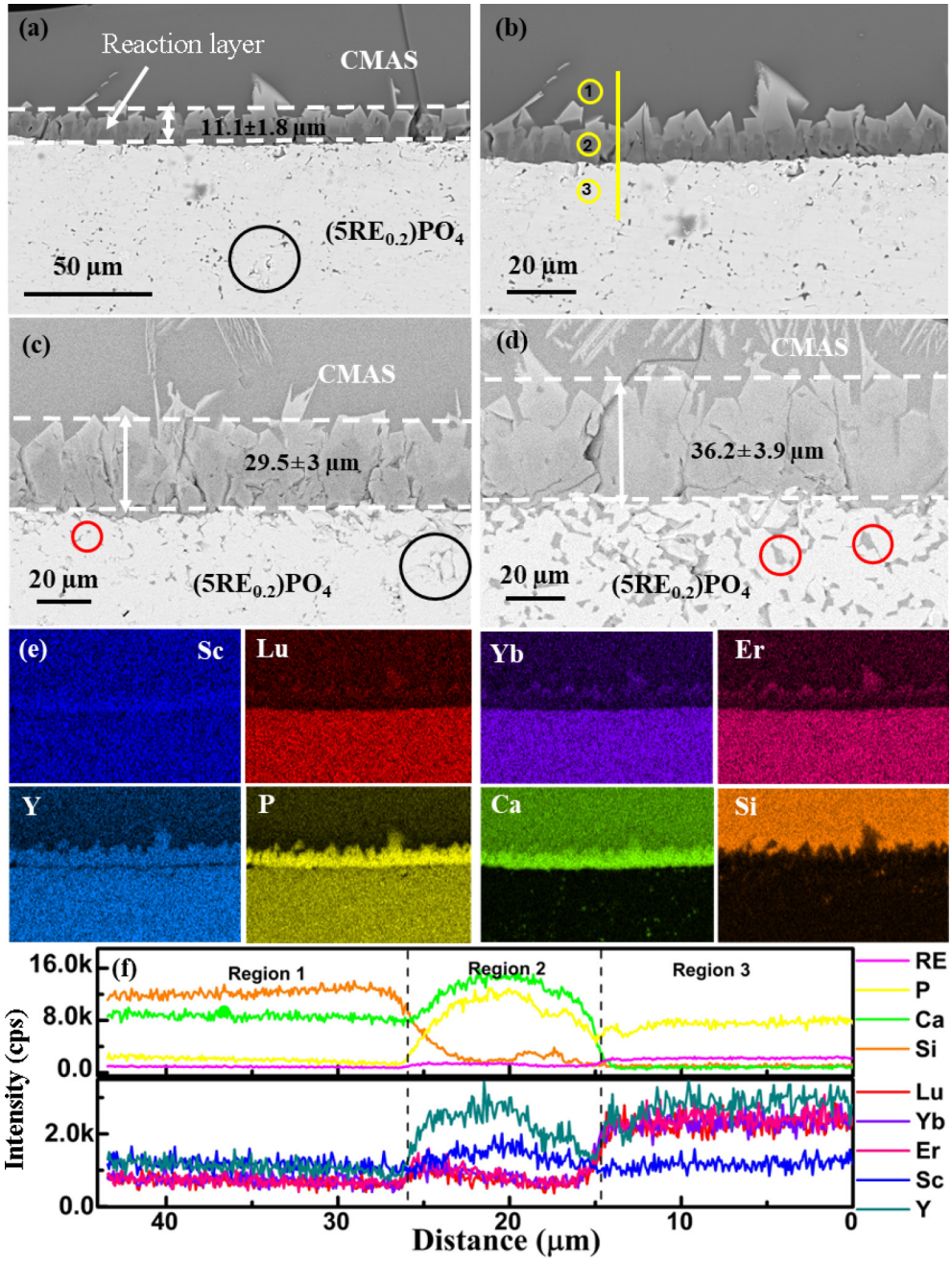

Fig. 15 Backscattered electron SEM images of cross-section of $(5RE_{0.2})PO_4$ pellet after CMAS reaction at 1300 °C for 5 h: (a) Low and (b) high magnification for (c) 45 h and (d) 96 h. (e) EDS mappings of $(5RE_{0.2})PO_4$ of area in (b) after CMAS reaction for 5 h at 1300 °C. (f) EDS line scan along yellow line denoted in (b).

in CMAS–$REPO_4$/$(5RE_{0.2})PO_4$ (RE = Sc, Lu, Yb, Er, and Y). The average thickness of the interfacial layer displays a linear correlation with the square root of time. All six RE phosphate–CMAS interactions show that the interfacial layer formation rate is higher at the beginning, and a reduction in growth can be found from 45 to 96 h compared with that between 5 and 45 h in all samples. The rate constants for interfacial layer formation are 3.2±0.1, 4.2±0.2, 3.7±0.5, 4.1±0.7, 5.3±0.4, and 3.5±0.5 $\mu m \cdot h^{-0.5}$ for $ScPO_4$, $LuPO_4$, $YbPO_4$, $ErPO_4$, YPO_4, and $HE(5RE_{0.2})PO_4$, respectively. The linear correlation in Fig. 16 indicates that a diffusion-controlled mechanism likely governs the interfacial layer formation during the CMAS reaction with the rare earth phosphate matrix [17]. Among all $REPO_4$ compounds, $ScPO_4$, which contains the smallest RE cation, has the slowest rate of interfacial layer formation, whereas YPO_4, with the largest RE cation, has the fastest formation rate of the interfacial layer. HE $(5RE_{0.2})PO_4$ has a formation rate that falls between those of $ScPO_4$ and YPO_4. This study revealed that the ionic radius of RE elements plays an important role in the stability of RE phosphates and interfacial reactions against CMAS attack [18]. Bryce *et al.* [27] studied the corrosion behavior of multicomponent $REPO_4$–CMAS ($40CaO–5MgO–5AlO_{1.5}–50SiO_2$) at 1300 °C and reported a rate constant of 5.4 $\mu m \cdot h^{-0.5}$. Using the same CMAS compositions as in this work, Ridley *et al.* [22] and Hu *et al.* [23] recently determined the rate constants for $YbPO_4$ and $LuPO_4$ to be 5.3 and 5.0 $\mu m \cdot h^{-0.5}$ after the CMAS reaction at1300 °C, respectively. These results indicate that our rate constants are comparable to those of previous studies.

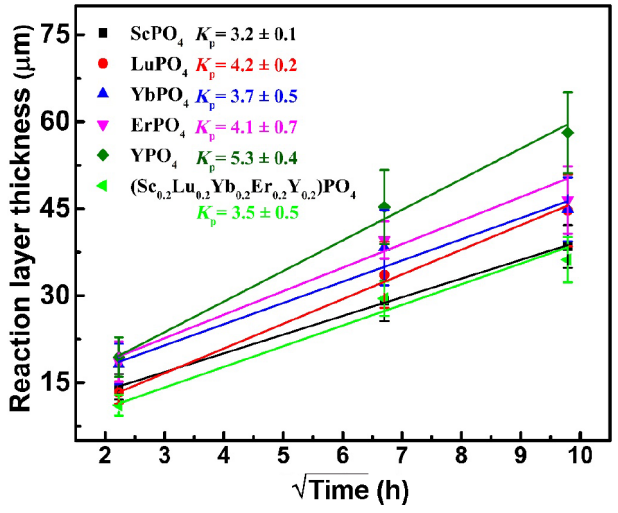

Fig. 16 Average reaction layer thickness vs. square root of time for $REPO_4$/$HE(5RE_{0.2})PO_4$–CMAS (RE = Sc, Lu, Yb, Er, and Y) interactions at 1300 °C.

3.5 Corrosion mechanisms and effects of ionic radius on CMAS-$REPO_4$/$(5RE_{0.2})PO_4$ interactions

The CMAS corrosion process in $REPO_4$ follows a dissolution-reprecipitation mechanism influenced by factors such as the type of RE species, temperature, and the Ca:Si ratio of CMAS [47]. The interaction of all five $REPO_4$ and $(5RE_{0.2})PO_4$ (RE = Sc, Lu, Yb, Er, and Y) with CMAS at 1300 °C for 5, 45, and 96 h results in the formation of a thick and continuous reaction layer that can hinder molten CMAS penetration (melting point ~1235 °C) into bulk pellets to a certain extent. The thickness and composition of these reaction layers are not the same for all six $REPO_4$ samples. The reaction layer is predominantly composed of the $Ca_8MgRE(PO_4)_7$ phase in all six samples, and the elemental maps show that the concentrations of RE elements vary throughout the region across the residual CMAS, reaction layer, and bulk pellet. However, Ca and P enrichment is observed in the reaction layer in $REPO_4$ (RE = Lu, Yb, and Er) [22]. The YPO_4–CMAS reaction layer is enriched in Ca (like other $REPO_4$), but P is not highly enriched, which differs from the other three rare earth phosphate (RE = Lu, Yb, and Er) reaction layers. The initial CMAS interaction with all $REPO_4$/$(5RE_{0.2})PO_4$ can be expressed as Reaction (5) [22,26]:

$$7REPO_4 + 8CaO + MgO \rightarrow Ca_8MgRE(PO_4)_7 + \text{RE-Si enriched CMAS glass} \quad (5)$$

The initial reaction triggers the creation of a reaction layer of $Ca_8MgRE(PO_4)_7$, as shown in Reaction (5). This process involves the dissolution of RE elements and P into the CMAS, followed by the reprecipitation of $Ca_8MgRE(PO_4)_7$ at the $REPO_4$/CMAS interface. However, over longer durations (45 and 96 h) of the CMAS reaction, the concentrations of CaO and MgO decrease in the residual molten CMAS, and those of RE and Si increase and reach a certain value, resulting in the formation of the disilicate ($RE_2Si_2O_7$) phase [22,23]. After 45 and 96 h of the CMAS reaction, open pores (i.e., without CMAS) are also observed in $ScPO_4$ and $LuPO_4$ (as shown in the SEM images with black circles in Figs. 10(c) and 10(c) and Figs. 11(c) and 11(d)). However, in some cases, we observed CMAS penetration below the reaction layer, as marked by red circles. This study indicates that the rapid formation of a dense and continuous reaction layer could suppress CMAS penetration into bulk pellets. However, in the case of the $HE(5RE_{0.2})PO_4$–CMAS corrosion test, after 96 h, the CMAS penetrated into the bulk pellet, as shown in the red circles in Fig. 15(d). Ridley *et al.* [22] and Hu *et al.* [23] reported that in xenotime RE phosphates, $REPO_4$–CMAS interactions at high temperatures formed dense, continuous, and thick reaction layers composed of mainly $Ca_8MgRE(PO_4)_7$ (RE = Lu and Yb) and disilicate phases present in the residual CMAS layer along with $Ca_2RE_8(SiO_4)_6O_2$ [22,23]. Our studies confirm that all xenotime $REPO_4$ (single and multicomponent) forms a continuous and thick reaction layer after CMAS ($C_{33}M_9A_{13}S_{45}$) interaction at 1300 °C. The reaction layer is mainly composed of a typical rhombohedral $Ca_8MgRE(PO_4)_7$ phase, and the thickness of this layer depends upon the ionic radius of RE elements.

Compared with the mono-/silicate-CMAS interaction, the $REPO_4$–CMAS interaction results in different phase evolution and reaction pathways. In particular, after the CMAS reaction, mono- and disilicates formed a RE-enriched $Ca_2RE_8(SiO_4)_6O_2$ phase [16,48]. The RE-enriched reaction layer formation for silicate-based EBCs contrasts with the Ca-enriched interfacial layer formation for RE phosphates, with the dominant phase being $Ca_8MgRE(PO_4)_7$. The RE:Ca ratios are 0.125 and 4 for $Ca_8MgRE(PO_4)_7$ and $Ca_2RE_8(SiO_4)_6O_2$, respectively. This indicates that in the $REPO_4$–CMAS interaction, relatively small amounts of RE are consumed to form the Ca-enriched $Ca_8MgRE(PO_4)_7$ phase. The RE:P ratio in $Ca_8MgRE(PO_4)_7$ is much less than 1, indicating that a significant amount of RE likely remains in the molten CMAS above the reaction layer. Our experimental EDS map and line scan results indicate that more RE and Si are present at the top of the reaction layer. Further CMAS penetration and RE element dissolution will need to pass through the dense interfacial layer, and diffusion-controlled kinetics are identified from the linear correlation of the layer thickness with the square root of the reaction time. After prolonged corrosion and the consumption of Ca near the region of the interfacial layer, Ca-depleted and RE-enriched disilicate can form with the accumulation of RE elements in residual CMAS. These results suggest that the corrosion resistance of phosphates is potentially greater than that of silicates. The enhanced CMAS corrosion for phosphates compared with silicates can also be inferred from the depth of CMAS penetration. For example, Webster and Opila [16] studied CMAS corrosion of $Yb_2Si_2O_7$ at 1300 °C and reported complete penetration of CMAS glass (through a 1 mm pellet) and high porosity and blister formation after 96 h of CMAS exposure.

The effects of the ionic radius on the reaction kinetics and the reaction layer thickness are clearly observed in this study. Among all these $REPO_4$ samples, YPO_4, with the largest atomic radius of Y, has a higher reaction rate constant for interfacial layer formation than the other five RE phosphates, and $ScPO_4$, with the smallest atomic radius of Sc, has a lower reaction rate constant for interfacial layer formation than the other elements do. Owing to the lanthanide contraction, the ionic radii of RE elements gradually decrease as one progresses across the lanthanide series (La–Lu and Sc). This reduction in ionic radius results in stronger atomic bonding within the crystal structure and thus enhanced bond strength, in which REEs are confined to a polyhedron of nearest neighbor oxygens. This enhanced bond strength could improve corrosion resistance in phosphates with smaller RE cations, as evidenced by smaller reaction layer thicknesses and less CMAS penetration. Owing to the larger ionic radius of Y^{3+} than those of the other lanthanides in this study, Y could be easily dissolved into the molten salt for the formation of the reaction layer under the same experimental conditions, resulting in a higher formation rate of interfacial layers in YPO_4 than in other phosphates. Furthermore, the YPO_4 sample also shows more CMAS penetration after 5 h of CMAS than the other $REPO_4$

samples do. Some grains are separated from the bulk YPO_4 pellet, and CMAS-filled pores are observed below the reaction layer (as shown in the EDS mappings in Fig. 14(e)). Additionally, it is well documented that Y^{3+} ions reduce the viscosity of molten CMAS, potentially promoting faster infiltration [49] than other $REPO_4$ ions (RE = Sc, Lu, Er, and Yb), despite their similar microstructures. Nevertheless, all $REPO_4$ pellets keep their main matrix unchanged, and there is no formation of pores within the matrix even after 96 h of the CMAS reaction at 1300 °C, unlike silicates [16].

Compared with its single-component counterparts, $(5RE_{0.2})PO_4$ formed the thinnest reaction layer after 96 h of CMAS corrosion. This could be a result of the slower dissolution rate of the RE elements in molten CMAS [47] for multicomponent phosphate due to structural disorder and, thus, slower atomic transport behavior. CMAS penetration occurs in $(5RE_{0.2})PO_4$ despite thinner reactor layer formation, and further design and composition optimization are necessary to develop multicomponent phosphates for EBC applications.

The effects of ionic size on corrosion resistance and reaction kinetics observed in this study are consistent with previous studies on monazite RE phosphates and silicates [20,21]. Wang *et al.* [21] investigated CMAS corrosion of three different monazite RE phosphates and reported that $LnPO_4$ (Ln = Nd, Sm, or Gd) with larger-sized lanthanides formed a dense and crack-free reaction layer of the apatite phase, which was mainly composed of $Ca_3Ln_7(PO_4)(SiO_4)_5O_2$. Previously, it was also observed that smaller cations are easier to incorporate into the apatite structure $Ca_{2+x}Ln_{8-x}(PO_4)_x(SiO_4)_{6-x}O_2$ [50,51]. Risbud *et al.* [52] reported a lower formation enthalpy for $Ca_{2+x}Ln_{8-x}(PO_4)_x(SiO_4)_{6-x}O_2$ with a reduced ionic size. Thus, among the three monazite phosphates, $GdPO_4$, with a smaller ionic size of Gd^{3+}, showed better CMAS resistance than $NdPO_4$ and $SmPO_4$ because of the rapid formation of a stable apatite reaction layer [21]. Jiang *et al.* [19] studied CMAS corrosion at 1200 °C for the monosilicate RE_2SiO_5 (RE = Y, Lu, Yb, Eu, Gd, and La) and reported that the ionic radii of RE elements play a vital role in the CMAS reaction. RE_2SiO_5 (RE = Y, Lu, and Yb) with a smaller RE^{3+} displays better CMAS resistance than RE_2SiO_5 (RE = Gd, Eu, and La) with a larger RE^{3+}. Similar trends are observed herein, where RE phosphates with a larger cation radius show more CMAS corrosion than those with a smaller cation radius.

3.6 Optical basicity (OB) and its effect on CMAS corrosion

Earlier research suggested that the smaller difference in OB value between EBC/thermal barrier coating (TBC) materials (rare earth silicate) and CMAS would be more desirable for a lower reaction [20]. Smaller differences in OB values suggest lower reactivity and vice versa [20,53]. The value of OB (Λ) represents the electron-accepting capability of metal cations and the electron-donating ability of O^{2-} ions in metal oxides. By utilizing OB theory, researchers can gain insights into the corrosive behavior of CMAS in various high-temperature environments, enabling a more detailed understanding of its impact on materials and potential mitigation strategies [20,42,53]. The OB value of a system can be calculated via Eq. (6) [53]:

$$\Lambda = \sum_i X_i \Lambda_i \tag{6}$$

where X_i and Λ_i represent the mole fraction of the ith part of the mixture and its OB value, respectively. The OB values of RE_2O_3, CMAS, and P_2O_5 are taken from Refs. [52–54] and shown in Table 2. Depending on the composition of CMAS, its OB value may vary between 0.49 and 0.65 [54].

Table 2 Λ for RE_2O_3, CMAS, $REPO_4$, and OB difference between $REPO_4$ and CMAS

Material	Λ	Material	Λ	$\Delta\Lambda_{REPO_4-CMAS}$
Y_2O_3	1.000 [54]	YPO_4	0.58125	−0.049
Yb_2O_3	0.940 [54]	$YbPO_4$	0.55875	−0.071
Er_2O_3	0.929 [55]	$ErPO_4$	0.55125	−0.075
Sc_2O_3	0.890 [54]	$ScPO_4$	0.54000	−0.090
Lu_2O_3	0.886 [55]	$LuPO_4$	0.53850	−0.091
P_2O_5	0.330 [56]	CMAS	0.63000 [20]	—

The OB values of $REPO_4$ are shown in Table 2, and the OB value difference between $REPO_4$ and CMAS ($\Delta\Lambda_{REPO_4-CMAS}$) decreases (i.e., the value becomes more negative) as the radius of the RE cation decreases. Consequently, the reactivity of $REPO_4$ toward CMAS corrosion decreases gradually from Y to Lu/Sc. Owing to the lower OB value of P_2O_5 (i.e., 0.33), the OB value of $REPO_4$ is smaller than that of rare earth silicate materials [20,53]. Hence, the difference in the OB value ($\Delta\Lambda_{REPO_4-CMAS}$) is negative. This OB difference analysis can serve as a rough screening tool for material selection for EBC applications. Our study revealed a relatively smaller difference in the OB values of CMAS and $REPO_4$ than those of the other silicates. This also indicates less severe corrosion between CMAS and $REPO_4$ than between CMAS and the other silicates. A study by Tina *et al.* investigated CMAS attack on RE_2SiO_5 (RE = Tm, Yb, Lu, Tb, Dy, and Ho) at 1300 °C, and their study revealed that the recession layer thickness was linearly related to the RE ionic radius (oxygen coordination number = 6) of RE_2SiO_5. Furthermore, the OB value difference between RE_2SiO_5 and CMAS linearly decreased as the ionic radius of RE decreased, and the progression of CMAS corrosion transitioned from severe to moderate and eventually to mild [20]. In another study, Kumar *et al.* [49] investigated the CMAS corrosion of yttrium aluminum garnet (YAG) and traditional yttria-stabilized zirconia (YSZ) for TBC applications. Their study revealed a smaller difference in the OB value between CMAS and YAG than that of YSZ, which helps minimize the damage to and reactivity of YAG.

In rare earth phosphates ($REPO_4$), the P^{5+} ion has a higher ionic potential than the Si^{4+} ion despite having a similar ionic radius. This higher ionic potential indicates a stronger bond between phosphorus and oxygen (P–O) than the Si–O bond. As a result, RE phosphates exhibit better CMAS corrosion resistance than RE silicates, primarily due to the stronger P–O bonds that provide enhanced stability in corrosive environments. In addition, phosphates with smaller RE cations may be better for CMAS corrosion resistance because of their stronger bonds and smaller rate constants for interfacial layer formation.

4 Conclusions

In this study, xenotime single-component $REPO_4$ and high-entropy $(5RE_{0.2})PO_4$ (RE = Sc, Lu, Yb, Er, and Y) were synthesized via a chemical route and consolidated into dense pellets via SPS. The phase stability and thermal properties of these materials were characterized, and their resistance to molten CMAS was thoroughly tested at 1300 °C for 5, 45, and 96 h. The critical material parameters that influence their thermal properties and CMAS corrosion resistance were identified. The key results of this study are as follows:

1) The average CTE of RE phosphates almost decreases linearly with increasing ionic radius of the RE elements. The CTE value of $(5RE_{0.2})PO_4$ is between those of $ScPO_4$ and $REPO_4$ (RE = Lu, Yb,

and Y), suggesting that Sc should be excluded when designing low-CTE multicomponent phosphates.

2) The thermal conductivity of single-component $REPO_4$ decreases with increasing ionic mass due to lattice distortion. $HE(5RE_{0.2})PO_4$ has a lower thermal conductivity than single-component $REPO_4$ does, which is attributed to its size and mass disorder.

3) CMAS interaction with xenotime RE phosphates leads to the formation of crystalline $Ca_8MgRE(PO_4)_7$, effectively impeding CMAS infiltration. The linear increase in the reaction layer thickness with the square root of the reaction time suggests a diffusion-controlled mechanism for all RE phosphates. However, due to the more negative Gibbs free energy of the reaction, $ScPO_4$ easily reacts with SiO_2, leading to the formation of a disilicate phase after 5 h of CMAS reactions. Prolonged CMAS reactions (45 and 96 h) resulted in the formation of disilicate ($RE_2Si_2O_7$) along with $Ca_8MgRE(PO_4)_7$ in all the samples.

4) The reaction layer thickness in single-component $REPO_4$ increases with increasing radius of the RE elements. Notably, after 96 h, $ScPO_4$, with the smallest ion, has the thinnest reaction layer, whereas YPO_4, with the largest ion, has the thickest reaction layer. The smaller-sized lanthanides resulting in improved CMAS corrosion resistance can also be attributed to enhanced bond strength. Compared with their single-component counterparts, $(5RE_{0.2})PO_4$ forms the thinnest reaction layer after 96 h of CMAS corrosion because of the slower mass transport of the mixed RE elements.

5) For rare earth phosphates, a greater negative difference in the OB value between $REPO_4$ and CMAS signifies greater corrosion resistance.

Combined with previous studies on monazite RE phosphates and silicates, our systematic investigation of single-component and multicomponent xenotime RE phosphates elucidates the important effects of the ionic radius of RE elements on their thermal properties, CMAS reaction kinetics, and corrosion resistance, offering valuable insights for the development of high-entropy materials as EBCs for protecting SiC–CMCs at high temperatures.

Acknowledgements

This work was supported as part of the DMREF: Machine Learning Accelerated Design and Discovery of Rare-earth Phosphates as Next Generation Environmental Barrier Coatings, a standard Grant funded by the Division of Materials Research, National Science Foundation under Award DMREF-2119423.

Competing interests

The authors have no competing interests to declare that are relevant to the content of this article.

References

[1] Padture NP. Advanced structural ceramics in aerospace propulsion. *Nat Mater* 2016, **15**: 804–809.

[2] Hardwicke CU, Lau YC. Advances in thermal spray coatings for gas turbines and energy generation: A review. *J Therm Spray Techn* 2013, **22**: 564–576.

[3] Jacobson NS. Corrosion of silicon-based ceramics in combustion environments. *J Am Ceram Soc* 1993, **76**: 3–28.

[4] Steibel J. Ceramic matrix composites taking flight at GE aviation. *AM Ceram Soc Bull* 2019, **98**: 30–33.

[5] Wang XL, Gao XD, Zhang ZH, *et al.* Advances in modifications and high-temperature applications of silicon carbide ceramic matrix composites in aerospace: A focused review. *J Eur Ceram Soc* 2021, **41**: 4671–4688.

[6] Park MS, Gu J, Lee H, *et al.* C_f/SiC ceramic matrix composites with extraordinary thermomechanical properties up to 2000 °C. *Nanomaterials* 2024, **14**: 72.

[7] Tejero-Martin D, Bennett C, Hussain T. A review on environmental barrier coatings: History, current state of the art and future developments. *J Eur Ceram Soc* 2021, **41**: 1747–1768.

[8] Xu Y, Hu XX, Xu FF, *et al.* Rare earth silicate environmental barrier coatings: Present status and prospective. *Ceram Int* 2017, **43**: 5847–5855.

[9] Poerschke DL, Hass DD, Eustis S, *et al.* Stability and CMAS resistance of ytterbium-silicate/hafnate EBCs/TBC for SiC composites. *J Am Ceram Soc* 2015, **98**: 278–286.

[10] Dong L, Yang WQ, Chen L, *et al.* Realizing the excellent oxidation resistance of an environmental barrier coating through aluminum surface modification. *J Adv Ceram* 2024, **13**: 976–986.

[11] Stolzenburg F, Kenesei P, Almer J, *et al.* The influence of calcium–magnesium–aluminosilicate deposits on internal stresses in $Yb_2Si_2O_7$ multilayer environmental barrier coatings. *Acta Mater* 2016, **105**: 189–198.

[12] Liu J, Zhang LT, Liu QM, *et al.* Calcium–magnesium–aluminosilicate corrosion behaviors of rare-earth disilicates at 1400 °C. *J Eur Ceram Soc* 2013, **33**: 3419–3428.

[13] Tejero-Martin D, Romero AR, Wellman RG, *et al.* Interaction of CMAS on thermal sprayed ytterbium disilicate environmental barrier coatings: A story of porosity. *Ceram Int* 2022, **48**: 8286–8296.

[14] Wei ZY, Meng GH, Chen L, *et al.* Progress in ceramic materials and structure design toward advanced thermal barrier coatings. *J Adv Ceram* 2022, **11**: 985–1068.

[15] Stokes JL, Harder BJ, Wiesner VL, *et al.* High-temperature thermochemical interactions of molten silicates with $Yb_2Si_2O_7$ and $Y_2Si_2O_7$ environmental barrier coating materials. *J Eur Ceram Soc* 2019, **39**: 5059–5067.

[16] Webster RI, Opila EJ. Mixed phase ytterbium silicate environmental-barrier coating materials for improved calcium–magnesium–alumino-silicate resistance. *J Mater Res* 2020, **35**: 2358–2372.

[17] Tian ZL, Zheng LY, Wang JM, *et al.* Theoretical and experimental determination of the major thermo-mechanical properties of RE_2SiO_5 (RE = Tb, Dy, Ho, Er, Tm, Yb, Lu, and Y) for environmental and thermal barrier coating applications. *J Eur Ceram Soc* 2016, **36**: 189–202.

[18] Tian ZL, Ren XM, Lei YM, *et al.* Corrosion of $RE_2Si_2O_7$ (RE = Y, Yb, and Lu) environmental barrier coating materials by molten calcium–magnesium–alumino–silicate glass at high temperatures. *J Eur Ceram Soc* 2019, **39**: 4245–4254.

[19] Jiang FR, Cheng LF, Wang YG. Hot corrosion of RE_2SiO_5 with different cation substitution under calcium–magnesium–aluminosilicate attack. *Ceram Int* 2017, **43**: 9019–9023.

[20] Tian ZL, Zhang J, Zheng LY, *et al.* General trend on the phase stability and corrosion resistance of rare earth monosilicates to molten calcium–magnesium–aluminosilicate at 1300 °C. *Corros Sci* 2019, **148**: 281–292.

[21] Wang F, Guo L, Wang CM, *et al.* Calcium–magnesium–alumina–silicate (CMAS) resistance characteristics of $LnPO_4$ (Ln = Nd, Sm, Gd) thermal barrier oxides. *J Eur Ceram Soc* 2017, **37**: 289–296.

[22] Ridley M, McFarland B, Miller C, *et al.* $YbPO_4$: A novel environmental barrier coating candidate with superior thermochemical stability. *Materialia* 2022, **21**: 101289.

[23] Hu XX, Xu FF, Li KW, *et al.* Thermal properties and calcium-magnesium–alumina–silicate (CMAS) resistance of $LuPO_4$ as environmental barrier coatings. *J Eur Ceram Soc* 2020, **40**: 1471–1477.

[24] Meng SJ, Guo L, Guo HB, *et al.* CMAS-phobic and infiltration-inhibiting protective layer material for thermal barrier coatings. *J Adv Ceram* 2024, **13**: 1254–1267.

[25] Bryce K, Majee BP, Huang LP, *et al.* A systematic study of thermomechanical properties and calcium–magnesium–aluminosilicate (CMAS) corrosion of multicomponent rare-earth phosphates. *J Adv Ceram* 2024, **13**: 1807–1822.

[26] Majee BP, Bryce K, Huang LP, *et al.* CMAS corrosion resistance of rare earth phosphates at high temperatures for environmental barrier coatings. *J Am Ceram Soc* 2025, **108**: e20251.
[27] Bryce K, Shih YT, Huang LP, *et al.* Calcium–magnesium–aluminosilicate (CMAS) corrosion resistance of high entropy rare-earth phosphate $(Lu_{0.2}Yb_{0.2}Er_{0.2}Y_{0.2}Gd_{0.2})PO_4$: A novel environmental barrier coating candidate. *J Eur Ceram Soc* 2023, **43**: 6461–6472.
[28] Sarker P, Harrington T, Toher C, *et al.* High-entropy high-hardness metal carbides discovered by entropy descriptors. *Nat Commun* 2018, **9**: 4980.
[29] Kaufmann K, Maryanovsky D, Mellor WM, *et al.* Discovery of high-entropy ceramics via machine learning. *NPJ Comput Mater* 2020, **6**: 42.
[30] Ranganathan S. Alloyed pleasures: Multimetallic cocktails. *Curr Sci* 2003, **85**: 1404–1406.
[31] Chang CC, Hsiao YT, Chen YL, *et al.* Lattice distortion or cocktail effect dominates the performance of tantalum-based high-entropy nitride coatings. *Appl Surf Sci* 2022, **577**: 151894.
[32] Zhang PX, Wang EH, Duan XJ, *et al.* Preparation and characterization of a novel monazite-type high-entropy $(La_{1/7}Ce_{1/7}Pr_{1/7}Nd_{1/7}Sm_{1/7}Eu_{1/7}Gd_{1/7})PO_4$ for thermal/environmental barrier coatings. *J Alloys Compd* 2023, **952**: 169978.
[33] Zhang PX, Duan XJ, Xie XC, *et al.* Xenotime-type high-entropy $(Dy_{1/7}Ho_{1/7}Er_{1/7}Tm_{1/7}Yb_{1/7}Lu_{1/7}Y_{1/7})PO_4$: A promising thermal/environmental barrier coating material for SiC_f/SiC ceramic matrix composites. *J Adv Ceram* 2023, **12**: 1033–1045.
[34] Chen ZL, Tian ZL, Zheng LY, *et al.* $(Ho_{0.25}Lu_{0.25}Yb_{0.25}Eu_{0.25})_2SiO_5$ high-entropy ceramic with low thermal conductivity, tunable thermal expansion coefficient, and excellent resistance to CMAS corrosion. *J Adv Ceram* 2022, **11**: 1279–1293.
[35] Min S, Blumm J, Lindemann A. A new laser flash system for measurement of the thermophysical properties. *Thermochim Acta* 2007, **455**: 46–49.
[36] Nikiforova GE, Ryumin MA, Gavrichev KS, *et al.* High-temperature thermodynamic properties of $LuPO_4$. *Inorg Mater* 2012, **48**: 841–844.
[37] Gavrichev KS, Ryumin MA, Tyurin AV, *et al.* Heat capacity and thermodynamic functions of $YbPO_4$ from 0 to 1800 K. *Inorg Mater* 2013, **49**: 701–708.
[38] Gavrichev KS, Ryumin MA, Tyurin AV, *et al.* Heat capacity and thermodynamic functions of pretulite $ScPO_4$(c) at 0–1600 K. *Geochem Int+* 2010, **48**: 390–397.
[39] Gavrichev KS, Ryumin MA, Tyurin AV, *et al.* Thermodynamic functions of erbium orthophosphate $ErPO_4$ in the temperature range of 0–1600 K. *Thermochim Acta* 2012, **535**: 1–7.
[40] Gavrichev KS, Ryumin MA, Tyurin AV, *et al.* Heat capacity and thermodynamic functions of xenotime YPO_4(c) at 0–1600 K. *Geochem Int* 2010, **48**: 932–939.
[41] Han J, Wang YF, Liu RJ, *et al.* Theoretical and experimental investigation of Xenotime-type rare earth phosphate $REPO_4$, (RE = Lu, Yb, Er, Y and Sc) for potential environmental barrier coating applications. *Sci Rep* 2020, **10**: 13681.
[42] Perrière L, Bregiroux D, Naitali B, *et al.* Microstructural dependence of the thermal and mechanical properties of monazite $LnPO_4$ (Ln = La to Gd). *J Eur Ceram Soc* 2007, **27**: 3207–3213.
[43] Zhang PX, Wang EH, Guo CY, *et al.* High-entropy rare earth phosphates ($REPO_4$, RE = Ho, Tm, Yb, Lu, Dy, Er and Y) with excellent comprehensive properties. *J Eur Ceram Soc* 2024, **44**: 1873–1879.
[44] Du AB, Wan CL, Qu ZX, *et al.* Thermal conductivity of monazite-type $REPO_4$ (RE = La, Ce, Nd, Sm, Eu, Gd). *J Am Ceram Soc* 2009, **92**: 2687–2692.
[45] Winter MR, Clarke DR. Oxide materials with low thermal conductivity. *J Am Ceram Soc* 2007, **90**: 533–540.
[46] Chen ZL, Tian ZL, Zheng LY, *et al.* Thermo-mechanical properties and CMAS resistance of $(Ho_{0.4}Yb_{0.3}Lu_{0.3})_2SiO_5$ solid solution for environmental barrier coating applications. *Ceram Int* 2023, **49**: 6429–6439.
[47] Qian B, Wang Y, Zu JH, *et al.* A review on multicomponent rare earth silicate environmental barrier coatings. *J Mater Res Technol* 2024, **29**: 1231–1243.
[48] Fan D, Zhong X, Zhang ZZ, *et al.* Interaction of high-entropy rare-earth monosilicate environmental barrier coatings subjected to corrosion by calcium–magnesium–alumino–silicate melts. *Corros Sci* 2022, **207**: 110564.
[49] Kumar R, Rommel S, Jiang C, *et al.* Effect of CMAS viscosity on the infiltration depth in thermal barrier coatings of different microstructures. *Surf Coat Tech* 2022, **432**: 128039.
[50] Cherniak DJ. Diffusion in accessory minerals: Zircon, titanite, apatite, monazite and xenotime. *Rev Mineral Geochem* 2010, **72**: 827–869.
[51] Cherniak DJ. Rare earth element diffusion in apatite. *Geochim Cosmochim Ac* 2000, **64**: 3871–3885.
[52] Risbud AS, Helean KB, Wilding MC, *et al.* Enthalpies of formation of lanthanide oxyapatite phases. *J Mater Res* 2001, **16**: 2780–2783.
[53] Nair RB, Brabazon D. Calcia magnesia alumino silicate (CMAS) corrosion attack on thermally sprayed thermal barrier coatings: A comprehensive review. *NPJ Mater Degrad* 2024, **8**: 44.
[54] Krause AR, Senturk BS, Garces HF, *et al.* $2ZrO_2{\cdot}Y_2O_3$ thermal barrier coatings resistant to degradation by molten CMAS: Part I, optical basicity considerations and processing. *J Am Ceram Soc* 2014, **97**: 3943–3949.
[55] Zhao XY, Wang XL, Lin H, *et al.* Electronic polarizability and optical basicity of lanthanide oxides. *Physica B* 2007, **392**: 132–136.
[56] Dimitrov V, Komatsu T. An interpretation of optical properties of oxides and oxide glasses in terms of the electronic ion polarizability and average single bond strength (review). *J Univ Chem Technol Metall* 2010, **45**: 219–250.